Broad ultra-potent neutralization of SARS-CoV-2 variants by monoclonal antibodies specific to the tip of RBD — Source link ⎋

Hang Ma, Yingying Guo, Haoneng Tang, Chien-Te Tseng ...+42 more authors

Institutions: Shanghai Jiao Tong University, Center for Infectious Disease Research and Policy, University of Texas Medical Branch, Chinese Center for Disease Control and Prevention

Topics: Epitope

Related papers:

- Structural Basis of a Human Neutralizing Antibody Specific to the SARS-CoV-2 Spike Protein Receptor-Binding Domain.

- Effects of Mutations in the Receptor-Binding Domain of SARS-CoV-2 Spike on its Binding Affinity to ACE2 and Neutralizing Antibodies Revealed by Computational Analysis

- Structural mechanism of SARS-CoV-2 neutralization by two murine antibodies targeting the RBD.

- Mutations in the SARS-CoV-2 Spike RBD are responsible for stronger ACE2 binding and poor anti-SARS-CoV mAbs cross-neutralization.

- A monoclonal antibody that neutralizes SARS-CoV-2 variants, SARS-CoV, and other sarbecoviruses

Share this paper: 𝐟 🐦 in ✉

Broad ultra-potent neutralization of SARS-CoV-2 variants by monoclonal antibodies specific to the tip of RBD

Running title: Potential clinical treatment to COVID-19 by SARS-CoV-2 variants

Hang Ma[1]*, Yingying Guo[3,4]*, Haoneng Tang[1]*, Chien-Te K. Tseng[5,6,7,8]*, Lei Wang[1], Huifang Zong[1], Zhenyu Wang[2], Yang He[2], Yunsong Chang[2], Shusheng Wang[9], Haiqiu Huang[9], Yong Ke[1], Yunsheng Yuan[1], Mingyuan Wu[1], Yuanyuan Zhang[3,4], Aleksandra Drelich[5], Kempaiah Rayavara Kempaiah[5], Bi-Hung Peng[6], Ailin Wang[9], Kaiyong Yang[9], Haiyang Yin[1], Junjun Liu[1], Yali Yue[1], Wenbo Xu[10], Shuangli Zhu[10], Tianjiao Ji[10], Xiaoju Zhang[11], Ziqi Wang[11], Gang Li[2], Guangchun Liu[2], Jingjing Song[2], Lingling Mu[2], ZongShang Xiang[2], Zhangyi Song[9], Hua Chen[9], Yanlin Bian[1], Baohong Zhang[1], Hui Chen[1], Jiawei Zhang[1], Yunji Liao[1], Li Zhang[9], Li Yang[11], Yi Chen[12], John Gilly[2,9], Xiaodong Xiao[2,9], Lei Han[2,13#], Hua Jiang[2,9#], Yueqing Xie[9#], Qiang Zhou[3,4#], Jianwei Zhu[1,2,9,13#]

[1]Engineering Research Center of Cell and Therapeutic Antibody, Ministry of Education, China; Shanghai Jiao Tong University, Shanghai 200240, China

[2]Jecho Biopharmaceuticals Co., Ltd. Tianjin 300467, China

[3]Center for Infectious Disease Research, Westlake Laboratory of Life Sciences and Biomedicine, Key Laboratory of Structural Biology of Zhejiang, School of Life Sciences, Westlake University, Hangzhou 310024, Zhejiang, China.

[4]Institute of Biology, Westlake Institute for Advanced Study, Hangzhou 310024, Zhejiang, China.

[5]University of Texas, Medical Branch, Departments of Microbiology and Immunology, Galveston, TX 77555, USA

[6]University of Texas, Medical Branch, Neurosciences, Cell Biology, and Anatomy, Galveston, TX 77555, USA

[7]University of Texas, Medical Branch, Pathology, Galveston, TX 77555, USA

[8]University of Texas, Medical Branch, Center for Biodefense and Emerging Disease, Galveston, TX 77555, USA

[9]Jecho Laboratories, Inc. Frederick, MD 21704, USA

[10]National Institute for Viral Disease Control and Prevention, China CDC, Beijing 102206, China

[11]Zhengzhou University People's Hospital; Henan Provincial People's Hospital, Department of Respiratory and Critical Care Medicine, Zhengzhou 450003, Henan, China

[12]Zhengzhou University People's Hospital; Henan Provincial People's Hospital, Clinical Research Service Center, Zhengzhou 450003, Henan, China

[13]Jecho Institute, Co., Ltd. Shanghai 200240, China

*These authors contributed equally: Hang Ma, Yingying Guo, Haoneng Tang, Chien-Te K. Tseng

#Correspondent authors: LH, lei.han@jechobio.com; HJ, hua.jiang@jecholabs.com; YX, yueqing.xie@jecholabs.com; QZ, zhouqiang@westlake.edu.cn; JZ, jianweiz@sjtu.edu.cn

Abstract

Severe acute respiratory syndrome coronavirus 2 (SARS-CoV-2) variants of concern (VOCs) continue to wreak havoc across the globe. Higher transmissibility and immunologic resistance of VOCs bring unprecedented challenges to epidemic extinguishment. Here we describe a monoclonal antibody, 2G1, that neutralizes all current VOCs and has surprising tolerance to mutations adjacent to or within its interaction epitope. Cryo-electron microscopy structure showed that 2G1 bound to the tip of receptor binding domain (RBD) of spike protein with small contact interface but strong hydrophobic effect, which resulted in nanomolar to sub-nanomolar affinities to spike proteins. The epitope of 2G1 on RBD partially overlaps with ACE2 interface, which gives 2G1 ability to block interaction between RBD and ACE2. The narrow binding epitope but high affinity bestow outstanding therapeutic efficacy upon 2G1 that neutralized VOCs with sub-nanomolar IC_{50} *in vitro*. In SARS-CoV-2 and Beta- and Delta- variant-challenged transgenic mice and rhesus macaque models, 2G1 protected animals from clinical illness and eliminated viral burden, without serious impact to animal safety. Mutagenesis experiments suggest that 2G1 could be potentially capable of dealing with emerging SARS-CoV-2 variants in future. This report characterized the therapeutic antibodies specific to the tip of spike against SARS-CoV-2 variants and highlights the potential clinical applications as well as for developing vaccine and cocktail therapy.

Introduction

Since the first Coronavirus Disease 2019 (COVID-19) case was diagnosed at the end of 2019, the severe acute respiratory syndrome coronavirus 2 (SARS-CoV-2) has caused more than 200 million confirmed infections and 4.5 million deaths in the following eighteen months, with no sign of stopping (https://ourworldindata.org/coronavirus)[1-6]. The hope-placed distribution of vaccines once appeared effectively controlling the virus spread. However, the antigenic evolution of SARS-CoV-2, especially in the spike (S) protein associated with receptor binding, alters the viral immunogenicity facilitating the virus's immune escape and crossing transmission barriers[7,8].

Receptor binding domain (RBD) on the S protein is a determinant that mediates the binding of SARS-CoV-2 to the angiotensin-converting enzyme 2 (ACE2). Neutralizing antibodies targeting RBD were proved to be effective[9-11]. Correspondingly, substitutions on RBD may reduce neutralizing efficacy[12-14]. Several variants, listed as Variant of Concern (VOC), featured with RBD substitutions and non-RBD mutations showed to have higher transmissibility and led to more severe illness[15-17], which has been causing great global dissemination concern. SARS-CoV-2 B.1.1.7 (Alpha) was first identified in United Kingdom in late summer of 2020 and rapidly became the dominant variant. This variant has nine mutations in the S protein, one of which is N501Y in RBD[18]. Alpha variant possesses a comparative transmission advantage, with a reproductive number 50% to 100% higher than other non-VOC lineages[1]. Vaccine-elicited neutralizing antibody responses were shown to be at risk of being desensitized by Alpha[19]. SARS-CoV-2 B.1.351 (Beta) has three substitutions in RBD, i.e., K417N, E484K, and N501Y. Incorporation of E484K empowers variants possible being completely resistant to plasma neutralization[20]. Mutations E484K together with K417N and N501Y largely contribute to the escape of Beta variant from convalescent and vaccine-induced sera[21,22]. SARS-CoV-2 P.1 (Gamma) shares three identical site-mutations in RBD with Beta variant, and their differences are that the substitution of K417 is threonine in Gamma variant, while is asparagine in Beta variant. Similarly, Gamma variant notably reduced susceptibility to antibody treatment and vaccine protection[23,24]. SARS-CoV-2 B.1.617.2 (Delta) was first reported in India and quickly spread globally in the first half of 2021. This strain has more than ten S protein mutations and two of them, L452R and T478K, are in RBD. Delta variant exhibits more extensive immunologic resistance than Alpha, escaping from many S protein antibodies targeting RBD and non-RBD epitopes[25,26]. Individuals who recovered from Beta and Gamma variants are more susceptible to be infected with Delta[27]. In addition to these VOCs, potential outbreaks of several variants have raised public concern, such as the recently rapidly spreading variant C.37 (Lambda)[28] and the new variant B.1.621 (Mu)[29]. The emergence of these variants, even possible hybrid variants, raises the risk of compromising the therapeutic effectiveness of vaccines and neutralizing antibodies that were previously developed[30,31].

Here we report our efforts on discovering neutralizing antibodies that provide extensive protection against the variants with global impact, especially the VOCs. We isolated RBD positive single B cells from convalescent individuals and cloned monoclonal antibodies (mAbs) within. After a series of programmed screening, several antibodies with remarkable neutralizing effect were panned out from the candidates (Fig. 1a). One of these antibodies,

133   designated as 2G1, efficiently neutralized all VOCs including widely spread Alpha, Beta,

134   Gamma, Delta variants and Cluster 5, a variant with Y453F substitution once caused public

135   concern due to the zoonotic characteristics. The antibody 2G1 was subsequently fully

136   characterized physic-chemically and biologically, as well as evaluated in potential in clinical

137   applications.

138

139   **Results**

140   Molecule discovery of 2G1

141   We collected blood samples from 20 convalescent individuals who were infected by SARS-

142   CoV-2 in February 2020. Peripheral blood mononuclear cells were enriched and sorted

143   with fluorescently labeled recombinant SARS-CoV-2 RBD (WA1/2020) protein (Fig. 1b).

144   Over 1200 B cells were isolated and more than 500 pairs of IgG antibody genes were

145   cloned by single-cell PCR. Of which, 375 are kappa subtype and 174 are lambda subtype

146   (Fig. 1c). 143 RBD binders were obtained after the ELISA-based preliminary screening

147   (Fig. 1d). In the following pseudovirus-based screening, three molecules, including 2G1,

148   displayed ultra-potent neutralization with IC_{50} less than 0.01 µg/mL (Fig. 1e). Antibody 2G1

149   stood out from these candidates after further investigation despite the binding and ACE2

150   blocking abilities were not remarkable (Supplementary information, Fig. S1a-b). In the

151   germline analysis of 33 candidates, 23 heavy chains were from IGHV3 and 18 light chains

152   were from IGKV1 (Supplementary information, Fig. S2). Six heavy chains, including 2G1,

153   were from IGHV3-53, which was reported having short complementarity-determining

154   region and with minimal affinity but high efficacy[32].

155   WA1/2020 RBD-mFc and S trimer proteins and pseudovirus were employed to further

156   confirm the antigen-binding and neutralizing ability of 2G1. Antibody 2G1 bound to RBD-

157   mFc and S trimer with EC_{50} of 0.016 µg/mL and 0.135 µg/mL (Fig. 2a-b) and neutralized

158   WA1/2020 pseudovirus with IC_{50} 0.0031 µg/mL (Fig. 2c), in line with the results of previous

159   screening. Affinity of monovalent 2G1 (Fab) to RBD was measured by surface plasmon

160   resonance (SPR). Relatively moderate dissociation constant (K_d) of 2G1 to WA1/2020 RBD

161   was determined as 1.05×10^{-3} s^{-1}. The rapid binding of 2G1 with association constant K_a

162    $= 2.55 \times 10^{6}$ Ms^{-1} offered a sub-nanomolar equilibrium dissociation constant (K_D) value of

163   0.41 nM (Fig. 2d). Next, the antibody 2G1 was moved to further characterization including

164   *in vitro* and *in vivo* biological activities as well as structural and mechanism investigation.

165

166   2G1 neutralizing SARS-CoV-2 variants

167   With the continuing spread of mutations, combating SARS-CoV-2 variants has become a

168   crucial task. We explored the effects of 2G1 on the mutations at several important sites

169   such as N439K, Y453F, E484K and N501Y in terms of blocking the ACE2-RBD interaction.

170   The IC_{50} of 2G1 blocking WA1/2020 RBD, N439K, Y453F, E484K and N501Y interacting

171   with ACE2 were 0.1504, 0.1050, 0.2225, 0.1951 and 0.1672 µg/mL, respectively (Fig. 3a).

172   To further study the S mutants of VOCs influence on blocking ability of 2G1, mutant trimeric

173   S proteins of VOCs were used in ACE2 blocking experiment. The IC_{50} of 2G1 were 0.0821,

174   0.1066, 0.1074, 0.1047, and 0.7973 µg/mL, corresponding to WA1/2020, Alpha, Beta,

175   Gamma, and Delta (Fig. 3b). We determined the affinities of 2G1 with various S trimers

176   using SPR. 2G1 Fab bound to S trimers with nanomolar affinities. K_D of its binding to

177　WA1/2020, Alpha, Beta, Gamma, Kappa, and Delta were 1.02, 0.86, 2.77, 2.30, 1.04, and

178　15.30 nM, respectively (Fig. 3c). The dissociation rate of 2G1/Delta (K_d = 4.27 × 10^{-2} s^{-1})

179　was increased as compared with WA1/2020 (K_d = 1.05 × 10^{-3} s^{-1}), which leads to the

180　decrease in affinity.

181　In pseudovirus neutralization assays, we found that antibody 2G1 robustly neutralized all

182　pseudoviruses, including D614G, Alpha, Beta, Gamma, Delta, and Cluster 5 variants (Fig.

183　4a-g, Supplementary information, Fig. S3) with low IC$_{50}$, especially 0.0005 μg/mL against

184　Gamma and 0.0002 μg/mL against Cluster 5. Live SARS-CoV-2 neutralization assay

185　results were consistent with those from experiments using pseudoviruses. Antibody 2G1

186　neutralized WA1/2020 live virus with IC$_{50}$ of 0.0240 μg/mL (Fig. 4h) while it was more

187　inclined to neutralize Alpha, Beta, and Gamma live virus, with IC$_{50}$ decrease about 1.7-fold

188　(0.0138 μg/mL), 5.2-fold (0.0046 μg/mL), and 3.0-fold (0.0079 μg/mL). In this assay, 2G1

189　had the same neutralizing activity (IC$_{50}$ = 0.0240 μg/mL) against Delta and WA1/2020.

190

191　*In vivo* protection in animal models

192　To evaluate *in vivo* antiviral efficacy of 2G1 against SARS-CoV-2 challenge, we performed

193　viral clearance assay employing both ACE2 transgenic mouse and rhesus macaque

194　models. In the transgenic mouse study, animals were challenged with high copies of 100

195　times of half lethal dose (LD$_{50}$) of SARS-CoV-2 WA1/2020, Beta, or Delta at day 0, followed

196　by three different 2G1 dose treatments (20, 6.7 or 2.2 mg/kg) or vehicle injection (PBS).

197　Four days post infection (dpi), four mice in each group including vehicle and differentially

198　treated groups were euthanized, and lungs and brains were collected for the titration of

199　viral load (Fig. 5a). Mice treated with vehicle developed an acute wasting syndrome and

200　quickly met the designed endpoint at 5 dpi. In contrast, WA1/2020 and Beta virus-infected

201　mice that received 20, 6.7 or 2.2 mg/kg treatments survived without losing any weight or

202　revealing any obvious signs of illness throughout the study (Fig. 5b-d). Delta virus-infected

203　mice in the 20 mg/kg group all survived throughout the trial period and had a good clinical

204　wellbeing score. In the same study, 55.6% mice in the 6.7 mg/kg group and 10% mice in

205　the 2.2 mg/kg group recovered back to healthy physiological condition (Fig. 5b-d) from the

206　virus challenge. The results indicated that at the range of 6.7 - 20 mg/kg 2G1 antibody

207　treatment was effective for animals to recover from the viral infection.

208　In the study of rhesus macaque animal model (Fig. 6a), the animals were infected with 10^5

209　TCID$_{50}$ of SARS-CoV-2 (2019-nCoV-WIV04) per animal and randomly divided into control

210　(vehicle injection), low-dose (10 mg/kg of 2G1), and high-dose (50 mg/kg of 2G1) groups,

211　with one male and one female in each group. Drugs were intravenously given 24 h post

212　infection. All animals in the two therapy groups had a high viral load of 10^6 copies/mL in

213　the throat swab at 1 dpi. After the drug injection, the viral titer was gradually decreased.

214　The throat virus was cleared at 3 dpi in one of the high-dose animals and at 4 dpi in the

215　remaining treated animals (Fig. 6b). One animal in the control group had an elevated viral

216　titer in the anal swab at 5 dpi, but no animals in the antibody treated groups showed this

217　trend until 7 dpi (Fig. 6c). In addition, we checked the viral distribution in lung, trachea, and

218　bronchus tissues. The virus was detectable in most areas of the lungs, in the tracheas, and

219　bronchi of the control animals. In the group treated with high-dose of the antibody, the virus

220　was present in right-middle, left-middle, and left-lower of the lungs, as well as left-bronchi.

221   In the low-dose group, the virus was only found in tracheas (Fig. 6d). Results from both
222   transgenic mouse and rhesus macaque studies showed a promising protective efficacy of
223   2G1, in consistent with the *in vitro* neutralization results.
224   We further investigated the Fc effector function of 2G1. Results showed that 2G1 had no
225   obvious antibody-dependent cellular cytotoxicity (ADCC) effect (not shown) but moderate
226   antibody-dependent cellular phagocytosis (ADCP) up to 35% (Supplementary information,
227   Fig. S4a). We hypothesize that the moderate ADCP may help the antigen presentation of
228   SARS-CoV-2. Pharmacokinetics (PK) study revealed the half-life of 2G1 in mice was 11.1
229   days (Supplementary information, Fig. S4b), similar to many therapeutic antibodies. Mice
230   treated with 15 mg/kg, 30 mg/kg, or 60 mg/kg showed no statistical changes in body weight,
231   white blood cell count, red blood cell count, hemoglobin, and platelets (Supplementary
232   information, Fig. S4c-g). Mice received 2G1 treatment had no evident pathological changes
233   in hearts, livers, spleens, lungs and kidneys (Supplementary information, Fig. S5).
234   Currently, Investigational New Drug-directed systematic safety assessment is ongoing to
235   support the pre-clinical safety of using 2G1 in human clinical trials. Toxicology study in non-
236   human primate showed that 2G1 was well tolerated at the maximum experimented dosage
237   of 200 mg/kg.
238
239   Cryo-EM structure of the complex between 2G1 and SARS-CoV-2 S protein
240   To investigate the binding mode of antibody 2G1 on S trimer, we solved the cryo-electron
241   microscopy (cryo-EM) structure of 2G1 in complex with S trimer at 2.7 Å resolution (Fig.
242   7a, Supplementary information, Fig. S6-7). Yet, the cryo-EM map density on the interface
243   between RBD and 2G1 were smeared. So, we performed local refinement
244   and improved the antibody-antigen interface resolution to 3.2Å, enabling reliable analysis
245   of the interactions between the RBD and 2G1 (Fig. 7b). In the S/2G1 complex, three solved
246   Fabs bound to trimeric S with all RBDs in the "down" position and the S protein in a locked
247   conformation[33,34] (Fig. 7a). There is an additional density in RBD domain of the structure,
248   which was reported as free fatty acid linoleic acid (LA) in a locked conformation[33].
249   For detailed analysis of the interface, antibody 2G1 binds to tip area of RBD of S trimer,
250   overlapping with the ACE2 binding site on RBD and offset from the major mutational
251   hotspots in VOCs. The heavy chain of 2G1 interacts with RBD mainly through three
252   complementarity-determining regions, named CDRH1 (residues 30 to 35), CDRH2
253   (residues 50 to 65), and CDRH3 (residues 98 to 111). The light chain of 2G1 participates
254   interaction mainly through two CDRs, CDRL1 (residues 23 to 36) and CDRL3 (residues 91
255   to 100) (Fig. 7b-e). The interface between RBD and 2G1 is stabilized by an extensive
256   hydrophobic interaction network. Phe486 on the RBD top loop interacts with Tyr33, Tyr52
257   on heavy chain and Tyr34, Tyr93, Trp99 on light chain through hydrophobic and/or π-π
258   interactions simultaneously (Fig. 7c). CDRH1 and CDRH3 of the 2G1 heavy chain were
259   positioned above the LA binding pocket in the adjacent RBD' (Fig. 7b and 7e). We further
260   compared 2G1 with three antibodies (S2E12, B1-182.1 and REGN10933), which have
261   similar patterns of epitope (Fig. 8a-c). Structural comparison reveals that the epitope for
262   2G1 partially overlaps with these three antibodies (S2E12, B1-182.1 and REGN10933),
263   but they have different binding directions (Fig. 8b). Besides, 2G1 has a relative narrow
264   binding epitope which may result less probability of losing neutralizing activity due to viral

265   mutagenesis (Fig. 8c).

266

267   Potential escape risk evaluation

268   To address the potential virus escape issue, we collected the high-frequency mutation sites
269   near the 2G1 binding epitope from GISAID database as of August 2021 (Fig. 9a), and
270   constructed a series of S protein sequences containing these mutations. The change in
271   binding ability of 2G1 was reflected by the normalized mean fluorescent intensity (MFI)
272   relative to the wild-type S protein in flow cytometry. Mutants 484K, 477N/484Q/490S, and
273   477R/478K/484K distinctly reduced 2G1 binding (Fig. 9b). Mutants 477N/490S,
274   477R/490S, 478K/484Q, and 484K/490S remarkably enhanced 2G1 binding (Fig. 9b). The
275   484K substitution is featured in variants Beta and Gamma. Although 484K alone leads to
276   a decreased binding ability of 2G1, trimeric S harbor all mutation sites only slightly
277   influenced the affinity of 2G1 (Fig. 3c). The 484K substitution leads to the loss of salt bridge
278   between Glu484 and ACE2 Lys31, resulting in the reduced affinity of ACE2[35]. It may be
279   one of the reasons why the activity of 2G1 even slightly improved in neutralizing Beta and
280   Gamma mutants. Another substitution in residue 484 with Gln (484Q) only slightly
281   weakened the binding of 2G1 (Fig. 9b). SARS-CoV-2 Delta variant possesses the T478K
282   substitution, which is a contact residue with 2G1. The single point mutation with T478K has
283   mildly decreased the 2G1 binding (Fig. 9b), which is consistent with the SPR data.
284   We also directly mutated the key interacting residues between RBD and 2G1 by alanine
285   substitution, though they are not high-frequency mutation sites. Only moderate decline in
286   2G1 interaction was found in several mutations, including 486A, 489A, 477A/487A, and
287   477A/489A (Fig. 9c). These results suggest that 2G1 could potentially be effective against
288   future SARS-CoV-2 variants.

289

290   **Discussion**
291   SARS-CoV-2 has no sign of stopping its transmission since the outbreak, and the
292   emergence of variants with increased transmissibility and capability of surveillance escape
293   has assisted its continued existence. Recently, the variant Delta has become an intensively
294   concerned strain due to its unparalleled transmissibility, which is embodied in the 1000
295   times higher viral load than the ancestral strain of SARS-CoV-2[6,36]. The high-frequency
296   mutation nature of SARS-CoV-2 necessitates the development of therapies with
297   breadth[37,38]. We screened antibodies with broad spectrum of neutralizing effects from
298   convalescent subjects. One of which, 2G1, showed excellent and extensive neutralization
299   to both ancestral SARS-CoV-2 WA1/2020 and VOCs at sub-nanomolar IC_{50} level. In the *in*
300   *vivo* study, transgenic mice infected by the WA1/2020- and Beta- were cured by antibody
301   2G1 at a dose as low as 2.2 mg/kg, as well as fully protected from Delta infection in the
302   range from 6.7 to 20 mg/kg, even when animals were challenged with 100 times LD_{50} of
303   viral load. These results indicate that 2G1 is a potent therapeutic antibody against the
304   broad spectrum of variants currently being concerned.
305   The cryo-EM structure of 2G1 in complex with the S protein revealed that 2G1 binds to the
306   tip of S trimer through small interface but strong hydrophobic effect. The strong
307   hydrophobic effect provides high affinity for 2G1, and the K_D of interaction with S trimers of
308   SARS-CoV-2 and VOCs ranges from 0.86 nM to 15.3 nM. SARS-CoV-2 variants Beta and

309 Gamma possess E484K and N501Y substitutions, which are adjacent to the epitope of
310 2G1. We correspondingly detected a slight decrease in the affinity of 2G1, from 1.02 nM
311 for WA1/2020 to 2.77 nM for Beta and 2.30 nM for Gamma. Surprisingly, 2G1 showed no
312 compromise in activity against Beta and Gamma in both pseudo- and live- viruses, and
313 both *in vitro* and *in vivo*. The dose of 2.2 mg/kg of 2G1 completely cleared the viral load in
314 Beta virus challenged transgenic mice, and the efficacy of which was as good as for
315 WA1/2020 virus challenged mice. The IC_{50} even improved in the *in vitro* live virus test,
316 decreased from 0.0240 µg/mL against WA1/2020 to 0.0046 µg/mL against Beta and 0.0079
317 µg/mL against Gamma. These results suggest that changes in affinity may not ultimately
318 determine the therapeutic effect of neutralizing antibodies, and various other factors could
319 be involved[35,39]. In addition, the small binding epitope reduces the probability of
320 interference between 2G1 and other RBD antibodies so that 2G1 can cooperatively work
321 with those antibodies to achieve a synergistic effect, for better responding to immunologic
322 evasion of SARS-CoV-2 variants.
323 Furthermore, the specific 2G1 antibody epitope of RBD tip is offset from mutational hot
324 spots and increases neutralization breadth covering new-onset VOCs. Variants Lambda
325 comprising L452Q/F490S and Mu comprising E484K/N501Y in RBD have recently raised
326 concerns[28,29]. Although residue 490 is nearing 2G1 epitope, our results suggested that
327 F490S did not cause significant affinity alteration. The E484K/N501Y substitution in variant
328 Mu is also seen in Beta and Gamma. In view of the good binding and neutralization of 2G1
329 against Beta and Gamma, we believe that 2G1 will likely be comparatively effective against
330 Mu. In addition, we directly mutated the amino acid residues adjacent to the epitope on
331 RBD by 2G1, as well as several residues that directly interact with 2G1, and found that
332 only few mutation groups may cause a significant weakening of the 2G1 binding ability.
333 Collectively, the model of 2G1 binding to the tip of S trimer provides a good reference for
334 developing vaccines and optimizing a better combination therapy.
335 The neutralizing antibody 2G1 has been manufactured under cGMP to support the
336 Investigational New Drug application. We would believe that antibody treatment with 2G1
337 will bring clinical benefit to COVID-19 patients.
338
339 **Materials and Methods**
340 B cells
341 Blood samples were obtained from patients who were recovered from COVID-19 for 10
342 weeks and had a negative nucleic acid test. Samples with serum antibody titer over 1 ×
343 10^6 were chosen for the peripheral blood mononuclear cells (PBMCs) separation using
344 Ficoll density gradient centrifugation method. B cells were enriched applying a human B
345 Cell Isolation Kit (Stemcell). Afterwards, B cells were then stained with APC-Alex700
346 labeled anti-CD19 (BD), BV421 labeled anti-CD27 (BD), BV510 labeled anti-IgG (BD),
347 Biotin labeled RBD (Sino Biological), PE labeled streptavidin (ThermoFisher) and 7AAD
348 (BD) Single memory B cells with potential SARS-CoV-2 antibody secretion were sorted out
349 by gating 7AAD⁻, CD19⁺, CD27⁺, IgG⁺, and RBD⁺ using a BD Aria III cell sorter with
350 fluorescence-activated cell sorting modules. B cells were suspended into lysis buffer and
351 quickly frozen. B cell mRNA was subsequently converted to cDNA by SuperScript III
352 Reverse Transcriptase (Invitrogen) and V gene were rescued by PCR. Linear Cassettes

353   were composed of CMV promoter V_H or V_L and polyA tail, and were used for expressing a

354   small amount of antibody for preliminary screening.

355

356   mAb preparation

357   Heavy chains and light chain genes were inserted separately into pcDNA3.4 and amplified

358   in *E. coli* DH5α. PureLink™ HiPure Plasmid Miniprep Kit (Invitrogen) was used for low

359   endotoxin plasmid preparation. Monoclonal antibodies were transiently expressed by co-

360   transfecting ExpiCHO-S cells (ThermoFisher) with heavy chain and light chain plasmids

361   using an ExpiCHO™ Expression System (Gibco). Cell culture was harvested after an 8- to

362   14- day incubation at 37℃ with humidified atmosphere of 8% CO_2 with shaking. Full-length

363   IgG was obtained by affinity purification utilizing a Protein A chromatography column (GE

364   Healthcare) in AKTA avant (Cytiva). For long-term storage, antibodies were kept in a

365   solution containing 10 mM Histidine-HCl, 9% trehalose, and 0.01% polysorbate 80.

366

367   293T-ACE2 cells

368   To obtain HEK-293T cells with stable expression of ACE2 protein, a lentiviral system

369   bearing ACE2 (Genbank ID: BAJ21180.1) gene was constructed. In brief, HEK-293T cells

370   (ATCC) with 70% - 80% confluence in a 10 cm dish were co-transfected with 12 μg of

371   plasmid pHIV-puro encoding RRE and ACE2 genes, 8 μg of plasmid psPAX2 encoding gag

372   and pol, and 4 μg of plasmid VSV-G encoding G glycoprotein of vesicular stomatitis

373   virus(VSVG) using Lipofectamine 3000 Reagent (Invitrogen). 12 h later, the medium was

374   changed to fresh DMEM (Gibco) supplemented with 10% FBS (Gibco) for another 48 h

375   culturing. Medium containing virus particles was harvested and concentrated using a

376   Lentivirus Concentration Kit (Genomeditech). The concentrated virus particles were used

377   to infect HEK-293T cells under selection pressure of 10 μg/mL puromycin (Beyotime

378   Biotechnology). The transfection efficiency was examined by flow cytometry using S1-mFc

379   recombinant protein (Sino Biological) as primary antibody and FITC-AffiniPure Goat Anti-

380   Mouse IgG (Jackson) as secondary antibody. The resulting bulk transfected population

381   was sorted on a BD FACSJazz Cell Sorter (BD) with the BD FACS™ Sortware. Cells with

382   top 1% fluorescence intensity were retained and expanded for subsequent use.

383

384   S protein over-expression cells

385   The coding sequence for full-length wild-type S protein (GenBank: QHD43416.1) from

386   Met1 to Thr1273 was inserted into plasmid pHIV-puro1.0, followed by an internal ribosome

387   entry site (IRES) and puromycin resistance gene. The lentiviruses were generated using

388   the HEK-293T packaging system as mentioned above. 500 μL of filtered lentivirus

389   supernatant was added in a 24-well plate with Jurkat cells (ATCC). After cell expansion

390   and selection with 10 μg/mL puromycin for one week, the positive S expression was

391   confirmed by flow cytometry.

392

393   Antigen-binding ELISA

394   Enzyme-linked immunosorbent assays (ELISA) were applied to study the binding ability of

395   antibodies with SARS-CoV-2 RBDs (Sino Biological) and S trimers (AcroBiosystems).

396   Antigens were diluted with ELISA Coating Buffer (Solarbio) to 1.0 μg/mL and immobilized

9

397   onto High Binding ELISA 96-Well Plate (BEAVER) with 100 µL per well overnight at 4℃.
398   Plates were washed 4 times with PBST (Solarbio) and blocked with 3% skim milk for 1 h
399   at 37℃. Then, serially diluted antibodies were added 100 µL per well and incubated at 37℃
400   for 1h. After pipetting off the unbound antibodies, plates were washed 4 times with PBST
401   and further incubated with 100 µL per well of goat anti-human IgG (Fc specific)-Peroxidase
402   antibody (1 : 5000 dilution, Sigma) for 1 h at 37℃. After a final 4 times washing with PBST,
403   the binding of antibodies with SARS-CoV-2 antigens were visualized by adding 100 µL
404   peroxidase substrate TMB Single-Component Substrate solution (Solarbio) and incubating
405   for 15 min in dark. The reaction was terminated by adding 50µL stop buffer (Solarbio) and
406   the plates were immediately submitted to an ELISA microplate reader (TECAN Infinite
407   M200 Pro) to measure the optical density (OD) at 450 nm. Data were analyzed with
408   GraphPad Prism Version 9.0.0 and EC_{50} values were determined using a four-parameter
409   nonlinear regression.

410

411   ACE2 competition ELISA
412   For experiments involving the competitive binding of antibodies to SARS-CoV-2 RBD or S
413   trimer, recombinant hACE2-Fc protein was first biotinylated using EZ-Link Sulfo-NHS-
414   Biotin (ThermoFisher) as the instruction described. SARS-CoV-2 RBD (Sino Biological), S
415   trimer (AcroBiosystems), mutated RBDs (Sino Biological), and mutated S trimers
416   (AcroBiosystems) were coated onto High Binding ELISA 96-Well Plate (BEAVER). In order
417   to obtain an optimized hACE2-Fc concentration for this experiment, the concentration-
418   dependent binding of biotinylated hACE2-Fc to coated SARS-CoV-2 antigens was
419   measured by performing a conventional receptor-binding ELISA. The EC_{80} of biotinylated
420   hACE2-Fc was calculated by the four-parameter nonlinear fitting. Antibodies were serially
421   diluted in 1% BSA (Sigma) and added 50 µL into the antigen coated plates. Biotinylated
422   hACE2-Fc at EC_{80} concentration was subsequently pipetted into. After incubation at 37℃
423   for 1 h, plates were 4 times washed with PBST and incubated with 100 µL of 1 : 2000
424   diluted Ultrasensitive Streptavidin−Peroxidase Polymer (Sigma). After further washing, 100
425   µL TMB was added, and followed by detection of the bound hACE2 in the microplate reader.
426   Four-parameter nonlinear regression fitting in GraphPad Prism Version 9.0.0 was applied
427   for result analysis.

428

429   Surface Plasmon Resonance (SPR)
430   The binding affinities of antibodies to SARS-CoV-2 RBD and S trimers (wild-
431   type/B.1.1.7/B.1.351/P.1/B.1.617.1/B.1.617.2) were tested using a BIAcore 8K system
432   (Cytiva) together with CM5 biosensor chips (Cytiva). Antigens were diluted in pH 5.0
433   Acetate (Cytiva) and covalently coupled on chips using an Amine Coupling Kit (Cytiva).
434   After reaching a 70 RU coupling level, the excess antigens were washed away and the
435   unbound sites were blocked with ethanolamine. Antibodies were 2-fold serially diluted from
436   1.250 µg/mL to 0.039 µg/mL in HBS-EP buffer (Cytiva) and then injected for 120 s at 30
437   µL/min. After that, the binding was dissociated with HBS-EP buffer for 120 s, followed by
438   chip regeneration with pH 1.5 Glycine (Cytiva). Parameters including K_a, K_d and K_D values
439   were calculated employing a monovalent analyte model with BIAevaluation software.

440

441   Pseudovirus neutralization

442   ACE2-293T cells were seeded in a white 96-well plate (Corning) at a density of 1×10^4

443   cells per well one night prior to use. Serially diluted antibodies were incubated with wild-

444   type (Yeasen) or mutant pseudoviruses (GENEWIZ) for 0.5 h at $37^\circ C$. Human ACE2-Fc or

445   other SARS-CoV-2 RBD specific antibodies were used as a positive control to validate data

446   collection in different panels of screening. Medium containing equal amount of

447   pseudoviruses but no antibodies was used as blank control. The culture medium of ACE2-

448   293T cells was removed and then replaced by the antibody-pseudovirus mixture. All

449   operations were conducted in the BSL-2 lab in Shanghai Jiao Tong University. After an

450   additional 48 h incubation, the luminescence of each well was measured using a ONE-

451   Glo™ Luciferase Assay System (Promega) in the Infinite M200 Pro NanoQuant (TECAN).

452   The acquired luminescence units were normalized to those of blank control wells. Dose-

453   dependent neutralization curves were fitted using a four-parameter nonlinear regression in

454   GraphPad Prism Version 9.0.0.

455

456   Plaque reduction neutralization

457   Plaque reduction neutralization test was performed using SARS-CoV-2 WA1/2020

458   (US_WA-1/2020 isolate), Alpha- (B.1.1.7/UK, Strain: SARS-CoV-

459   2/human/USA/CA_CDC_5574/2020), Beta-(B.1.351/SA, Strain: hCoV-19/USA/MD-

460   HP01542/2021), Gamma- (P.1/Brazil, Strain: SARS-CoV-2/human/USA/MD-MDH-

461   0841/2021), and Delta-variants (B.1.617.2/Indian, Strain: GNL-751, a recently isolated

462   strain from Galveston County, Texas) at Galveston National Laboratory at University of

463   Texas Medical Branch at Galveston, Texas. Briefly, antibodies were 3-fold serially diluted

464   in MEM medium (Gibco) from 20 μg/mL for preparing the working solution. The dilutions

465   were mixed with equal volume of 100 $TCID_{50}$ virus in two replicates and incubated at room

466   temperature for 1 h. The mixture was then added into a 96-well plate covered with Vero

467   cells. Blank controls and virus infection controls were set up simultaneously. After

468   incubation at $37^\circ C$, 5% CO_2 for 3 days, cytopathic effect (CPE) was observed under

469   microscope and plaques were counted for efficacy evaluation. Wells with CPE changes

470   are recorded as "+", otherwise recorded as "-". IC_{50} values were calculated according to

471   the following equation: IC_{50} = Antilog (D - C × (50 - B) / (A - B)). Where A indicates the

472   percentage of inhibition higher than 50%, B indicates the percentage of inhibition less than

473   50%, C is $\log_{10}$ (dilution factor), D is $\log_{10}$ (Sample concentration which the inhibition is less

474   than 50%.

475

476   ACE2 transgenic mouse protection

477   AC70 human ACE2 transgenic mice (Taconic Biosciences) were divided into control (100

478   μL PBS) and treatment (20, 6.7, or 2.2 mg/kg of 2G1, 100 μL) groups, with 14 in each

479   group. Animal studies were carried out at Galveston National Laboratory at University of

480   Texas Medical Branch at Galveston, Texas, an AAALAC accredited (November 24, 2020)

481   and PHS OLAW approved (February 26, 2021) high-containment National Laboratory,

482   based on a protocol approved by the Institutional Animal Care and Use Committee at

483   UTMB at Galveston. Mice were challenged with 100 LD_{50} of SARS-CoV-2 (US_WA-1/2020

484   isolate), Beta-(B.1.351/SA, Strain: hCoV-19/USA/MD-HP01542/2021), or Delta-variants

11

485   (B.1.617.2/Indian, Strain: GNL-751, a recently isolated strain from Galveston County,

486   Texas), provided through World Reference Center for Emerging Viruses and Arboviruses

487   (WRCEVA) were used in the study. The first dose of antibody 2G1 and PBS were given 4

488   h post infection; and the second and third were given 2 days and 4 days post infection.

489   Mice were clinically observed at least once daily and scored based on a 1 to 4 grading

490   system that describes the clinical wellbeing. In the standardized 1 to 4 grading system,

491   score 1 is healthy; Score 2 is with ruffled fur and lethargic; Score 3 is with additional clinical

492   sign such as hunched posture, orbital tightening, increased respiratory rate, and/or > 15%

493   weight loss; Score 4 is showing dyspnea and/or cyanosis, reluctance to move when

494   stimulated, or ≥ 20% weight loss that need immediate euthanasia. Four mice in each group

495   were euthanized at 4 days post infection for assessing viral loads and histopathology of

496   lung and brain. The remaining 10 mice were continue monitored for morbidity and mortality

497   for up to 12 days post infection.

498

499   Rhesus macaque protection

500   Rhesus macaques at six to seven years old were purchased from Hubei Tianqin

501   Biotechnology Co., Ltd. All animal procedures and operations were approved by the ethical

502   committee of Wuhan Institute of Virology, Chinese Academy of Sciences. SARS-CoV-2

503   strain 2019-nCoV-WIV04 (GISAID number: EPI_ISI_402124) was isolated from the

504   bronchoalveolar lavage fluid of a patient who was infected COVID-19 in Wuhan in

505   December 2019. Rhesus macaques were randomly divided into control group, low-dose

506   (10 mg/kg of 2G1) and high-dose (50 mg/kg of 2G1) groups with one male and one female

507   in each. Animals were endotracheally infected with 4 mL of 1×10^5 TCID50 virus. Antibody

508   2G1 and PBS were intravenously given 24 h after infection. Rhesus macaques were

509   monitored for disease-related changes during the period. Body weight and temperature

510   were measured every day, and throat swab and anal swab samples were collected for virus

511   titrating. Animals were euthanized at 7 dpi and tissue samples were collected for virus

512   examining. Viral RNA was extracted using the QIAamp Viral RNA Mini Kit (Qiagen). A one-

513   step real-time quantitative PCR was used to quantify the viral RNA according to the

514   supplier's instructions (HiScript® II One Step qRT-PCR SYBR® Green Kit, Vazyme Biotech

515   Co., Ltd) together with primers for the RBD gene (RBD-qF1: 5'-CAATGGTTAAGGCAGG-

516   3'; RBD-qR1: 5'-CTCAAGGTCTGGATCACG-3').

517

518   Antibody-Dependent Cellular Phagocytosis (ADCP)

519   In ADCP experiment, CD14^{+} monocytes (Allcells) were cultured and differentiated for 7

520   days to obtain macrophage cells. Macrophages were labeled with violet dye

521   (ThermoFisher), and Jurkat cells with stable SARS-CoV-2 S expression were labeled with

522   CFSE dye (ThermoFisher). 75,000 Jurkat cells were added to macrophage cells in a 96-

523   well plate in the presence of 2G1 or the isotype control antibody. After incubating at 37℃

524   for 30 mins, the macrophages were digested and fixed with 4% paraformaldehyde, and the

525   proportion of double-positive cell populations was analyzed by flow cytometry.

526

527   Pharmacokinetic study and toxicity test

528   For the pharmacokinetic study, BALB/c mice were tail intravenously injected with 2G1 (15,

529   30, or 60 mg/kg), or equivalent volume of PBS. Three males and three females were in
530   each subset. Blood samples were collected 0.5 h, 6 h, 1 d, 2 d, 4 d, 7 d, 10 d, 15 d, 21 d,
531   and 28 d after injection. Serum 2G1 concentration was quantified using ELISA. Briefly,
532   Mouse Anti-human IgG Lambda (SouthBiotech) at 2 μg/mL was coated in ELISA plates.
533   Serum samples and antibody 2G1 control were added into the plates and incubated for 1
534   h. After washing, a Goat Anti-human Fc HRP (Sigma) was used as secondary antibody
535   with 1:6000 dilutions. After the chromogenic reaction by the HRP substrate (Solarbio), the
536   plates were read at 450 nm.
537   Crlj:CD1(ICR) mice were randomly divided into control (PBS), 15 mg/kg, 30 mg/kg, and 60
538   mg/kg groups for testing the *in vivo* toxicity of 2G1, with three males and three females
539   each group. Body weight was tracked every two days. Blood samples were collected 14
540   days after administration and mice were subsequently euthanized for tissue damage
541   detection. Blood indicators including white blood cell count, red blood cell count,
542   hemoglobin, and platelets were measured in multiple automated hematology analyzer
543   (Sysmex XT-2000iV). Pathological changes of hearts, livers, spleens, lungs and kidneys
544   were examined by hematoxylin-eosin (HE) staining.
545
546   Expression and purification of S protein
547   The prefusion S extracellular domain (1-1208 a.a) (Genbank ID: QHD43416.1) was cloned
548   into the pCAG vector (Invitrogen) with six proline substitutions at residues 817, 892, 899,
549   942, 986 and 987[39], a "GSAS" substitution (instead of "RRAR") at residues 682 to 685 and
550   a C-terminal T4 fibritin trimerization motif followed by one Flag tag.
551   This recombinant S protein was overexpressed using the HEK 293F mammalian cells
552   (Invitrogen) at 37℃ under 5% CO_2 in a Multitron-Pro shaker (Infors, 130 rpm). For secreted
553   S protein production, about 1.5 mg of the plasmid was premixed with 3 mg of
554   polyethylenimines (PEIs) (Polysciences) in 50 mL of fresh medium for 15 mins before
555   adding to cell culture, and transiently transfected into the cells, when the cell density
556   reached 2.0 ×10^6 cells/mL. Cells were removed by centrifugation at 4000×g for 15 mins
557   and cell culture supernatant was collected sixty hours after transfection. The secreted S
558   proteins were purified by anti-FLAG M2 affinity resin (Sigma Aldrich). After loading two
559   times, the anti-FLAG M2 resin was washed with the wash buffer containing 25 mM Tris (pH
560   8.0), 150 mM NaCl. The protein was eluted with the wash buffer plus 0.2 mg/mL flag
561   peptide. The eluent was then concentrated and subjected to gel filtration chromatography
562   (Superose 6 Increase 10/300 GL, GE Healthcare) in buffer containing 25 mM Tris (pH 8.0),
563   150 mM NaCl. The peak fractions were collected and concentrated to incubate with mAb.
564   The purified S protein was mixed with the 2G1 at a molar ratio of about 1:5 for one hour,
565   respectively. Then the mixture was subjected to gel filtration chromatography (Superose 6
566   Increase 10/300 GL, GE Healthcare) in buffer containing 25 mM Tris (pH 8.0), 150 mM
567   NaCl. The peak fractions were collected for EM analysis.
568
569   Cryo-EM sample preparation, data collection and data processing
570   The peak fractions of complex were concentrated to about 2.5 mg/mL and applied to the
571   grids. Aliquots (3.3 μL) of the S/2G1 complex were placed on glow-discharged holey
572   carbon grids (Quantifoil Au R1.2/1.3). The grids were blotted for 2.5 s or 3.0 s and flash-

573   frozen in liquid ethane cooled by liquid nitrogen with Vitrobot (Mark IV, ThermoFisher). The
574   prepared grids were transferred to a Titan Krios operating at 300 kV equipped with Gatan
575   K3 detector and GIF Quantum energy filter. Movie stacks were automatically collected
576   using AutoEMation[40], with a slit width of 20 eV on the energy filter and a defocus range
577   from -1.2 μm to -2.2 μm in super-resolution mode at a nominal magnification of 81,000×.
578   Each stack was exposed for 2.56 s with an exposure time of 0.08 s per frame, resulting in
579   a total of 32 frames per stack. The total dose rate was approximately 50 e$^-$/Å^2 for each
580   stack. The stacks were motion corrected with MotionCor2[41] and binned 2-fold, resulting in
581   a pixel size of 1.087 Å/pixel. Meanwhile, dose weighting was performed[42]. The defocus
582   values were estimated with Gctf[43].
583   Particles for S in complex with 2G1 were automatically picked using Relion 3.0.6[44-47] from
584   manually selected micrographs. After 2D classification with Relion, good particles were
585   selected and subject to two cycle of heterogeneous refinement without symmetry using
586   cryoSPARC[48].The good particles were selected and subjected to Non-uniform Refinement
587   (beta) with C1 symmetry, resulting in the 3D reconstruction for the whole structures, which
588   was further subject to 3D auto-refinement and post-processing with Relion. For interface
589   between S protein of SARS-CoV-2 and 2G1, the dataset was subject to focused refinement
590   with adapted mask on each RBD-2G1 sub-complex to improve the map quality. The
591   dataset of similar RBD-2G1 sub-complexes were combined if possible and necessary. The
592   re-extracted dataset was 3D classified with Relion focused on RBD-2G1 sub-complex.
593   Then the good particles were selected and subject to focused refinement with Relion,
594   resulting in the 3D reconstruction of better quality on RBD-2G1 sub-complex. The
595   resolution was estimated with the gold-standard Fourier shell correlation 0.143 criterion[49]
596   with high-resolution noise substitution[50]. Refer to Supplementary information, Fig. S6-7
597   and Table S1 for details of data collection and processing.
598   For model building of the complex of S of SARS-CoV-2 with 2G1, the atomic model of the
599   S in complex 4A8 (PDB ID: 7C2L) were used as templates, which were molecular dynamics
600   flexible fitted[51] into the whole cryo-EM map of the complex and the focused-refined cryo-
601   EM map of the RBD-2G1 sub-complex, respectively. A Chainsaw[52] model of the 2G1 was
602   first obtained using the 4A8 as a template, which was further manually adjusted based on
603   the focused-refined cryo-EM map of the RBD-2G1 sub-complex with Coot[53]. Each residue
604   was manually checked with the chemical properties taken into consideration during model
605   building. Several segments, whose corresponding densities were invisible, were not
606   modeled. Structural refinement was performed in Phenix[54] with secondary structure and
607   geometry restraints to prevent overfitting. To monitor the potential overfitting, the model
608   was refined against one of the two independent half maps from the gold-standard 3D
609   refinement approach. Then, the refined model was tested against the other map. Statistics
610   associated with data collection, 3D reconstruction and model building were summarized in
611   Supplemental information, Supplementary information, Table S1.
612
613   Binding to S mutants on cell surface
614   Plasmids encoding full length SARS-CoV-2 S (GenBank ID: QHD43416.1) with one or
615   more mutation sites were carried into HEK-293T cells using lipofectamine 3000
616   (ThermoFisher) according to the manufacturer's instruction. After 48 hours, cells were

14

617 disassociated from the plates using a Cell Dissociation Buffer (ThermoFisher) followed by
618 washing with PBS. Antibody 2G1 at 10 μg/ml was added into cells for a 30 min incubation.
619 Subsequently, cells were washed and incubated with Alexa Fluor 647 labeled Goat anti-
620 Human IgG (ThermoFisher) for 30 mins. After final washing, signals were acquired in flow
621 cytometer (BD) and the binding ability to S mutants were evaluated by mean fluorescent
622 intensity (MFI).
623

Acknowledgments

645

Author Contributions

647 LH, HM designed and conducted experiments on antibody binding activities, antibody
648 neutralizing experiments using pseudovirus system and drafted manuscript. LH, HT, HZ,
649 LW, YK, YY, HY, HuiC, JZhang, YL conducted experiments on molecular discovery from
650 blood sample to antibodies and characterization. MW, JL, YYue designed and executed
651 animal study on metabolic profile and toxicology. CKT, AD, KRK, BHP designed and
652 executed *in vitro* and *in vivo* study on virus neutralizing activity. XX provided technical
653 instructions on antibody screening from B cells. JG provided critical discussions and
654 manuscript editing. YX, HJ coordinated project on molecular discovery, characterization,
655 preparation, and provided critical discussions on *in vitro* and *in vivo* animal study on virus
656 neutralization. XZ, ZW, LY, YChen coordinated blood sample collection from convalescent
657 individuals and facilitated B-cell screening. ZW, YH, YChang, GL, GcL, JJS, LLM, ZX
658 conducted sample preparation, quality control, and product characterization. QZ conceived
659 the project on structure analysis. YG designed and did the cryo-EM experiments. YZ solved
660 the cryo-EM structures and YG and YZ analyzed the cryo-EM structures and made figures.

661 SW, HH, AW, KY, ZS, HuaC, LiZ conducted experiments on antibody expression, analytical
662 development, and characterization. WX, SZ, TJ, conducted *in vitro* virus neutralizing
663 assays. YB, BZ coordinate project activities and provided critical discussion. JZhu
664 designed the overall project, organized and coordinated activities from all participating
665 institutes, and revised manuscript.
666
667 **Conflict of Interest**
668 We declare that none of the authors have competing financial interests.
669
670
671
672
673
674
675
676
677
678
679
680
681
682
683
684
685
686
687
688
689
690
691
692
693
694
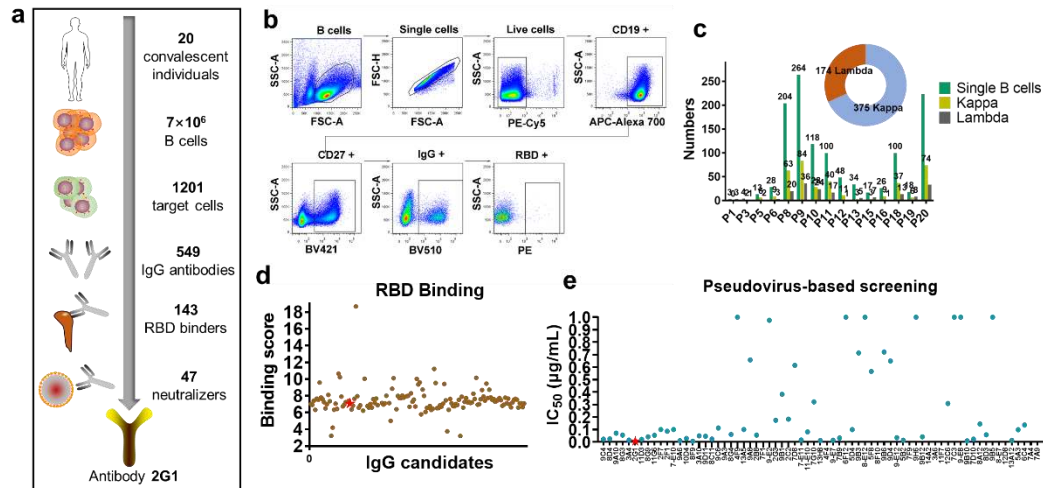
Fig. 1 Cell isolation, antibody cloning, and candidate panning. a, Isolation strategy of highly potent neutralizing antibodies as depicted by a diagram. **b,** RBD-specific B cells were isolated from convalescent subjects of SARS-CoV-2 infection by fluorescence-activated cell sorting. The 7ADD⁻/CD19⁺/CD27⁺/IgG⁺/RBD⁺ gate is shown and highlighted in the boxes. **c,** Statistics of the number of paired antibodies from each subject, as well as the number of kappa and lambda subtypes. **d,** Binding scores of antibody candidates against SARS-CoV-2 RBD as measured by ELISA and scores higher than 2 are presented. 2G1 is highlighted in red. **e,** Candidate panning using a WA1/2020 pseudovirus-based screening model. Antibodies were 10-fold serially diluted from 10^1 µg/mL to 10^{-4} µg/mL.

715
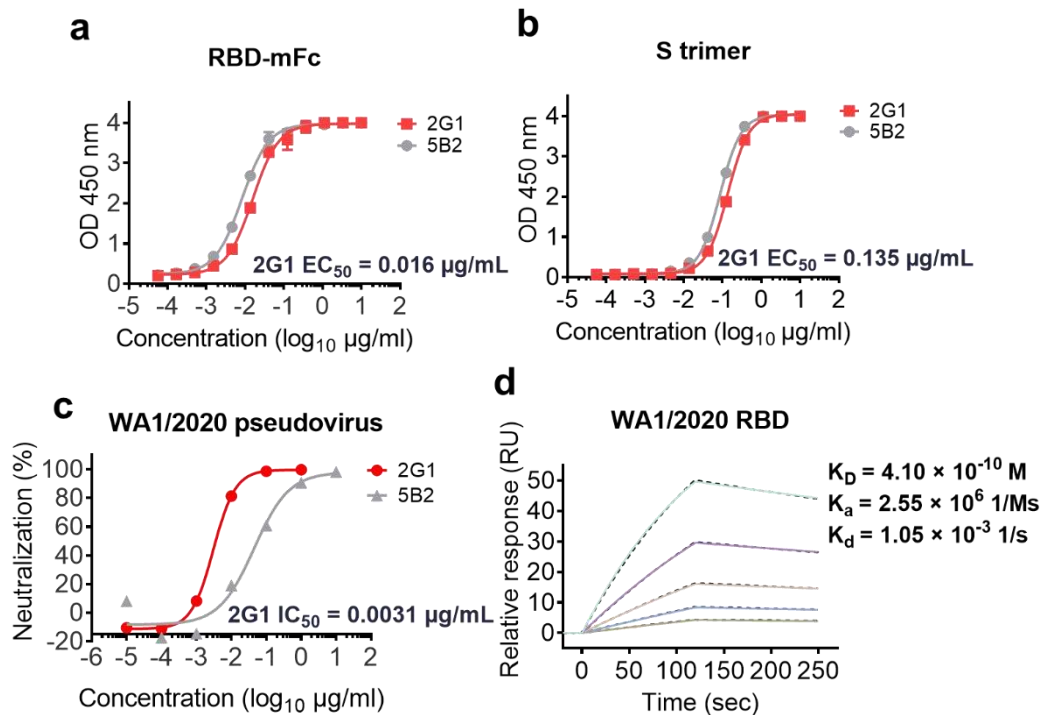
Fig. 2 Characterization of 2G1 using WA1/2020 related S and RBD proteins and pseudovirus. a-b, 2G1 concentration-dependently binds to RBD-mFc (**a**) and S trimer (**b**) of SARS-CoV-2 in ELISA test. A neutralizing antibody 5B2 targeting SARS-CoV-2 RBD was used as control. Values from two replicates are shown as mean ± S.D. **c,** Serial ten-fold-diluted 2G1 was incubated with SARS-CoV-2 WA1/2020 pseudovirus and used to infect 293T-ACE2 cells. After a 48 h incubation, the infection was quantified using a fluorescence detection kit. **d,** Binding kinetics of 2G1 to SARS-CoV-2 RBD in SPR. Serial dilutions of 2G1 Fab were flowed through a chip fixed with RBD recombinant protein. The kinetics data were fitted with results from different concentrations.
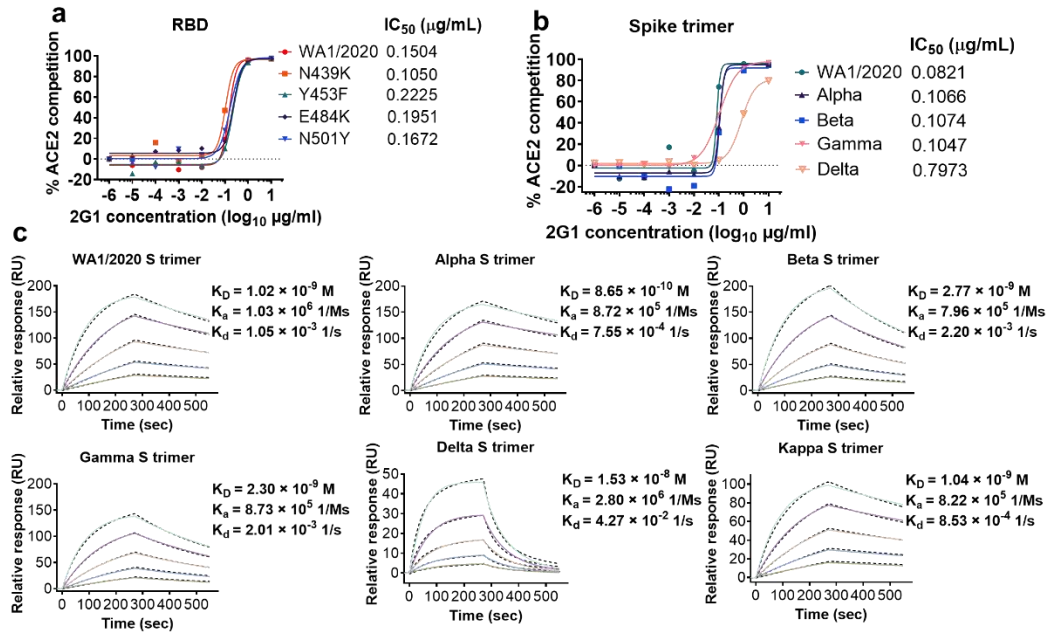
Fig. 3 Binding and blocking characteristics of 2G1 to SARS-CoV-2 variants. a-b, 2G1 competitively blocked the ACE2 binding to single point mutant RBD proteins (**a**) and VOC S trimers (**b**). **c,** Affinity analysis of 2G1 bound to S trimers of SARS-CoV-2 WA1/2020, Alpha, Beta, Gamma, Kappa and Delta by SPR. Chips fixed with S trimers were loaded on a BIAcore 8K system. 2G1 Fab varied from 1.250 µg/mL to 0.039 µg/mL were injected over the chips for measuring the real-time association and dissociation parameters.
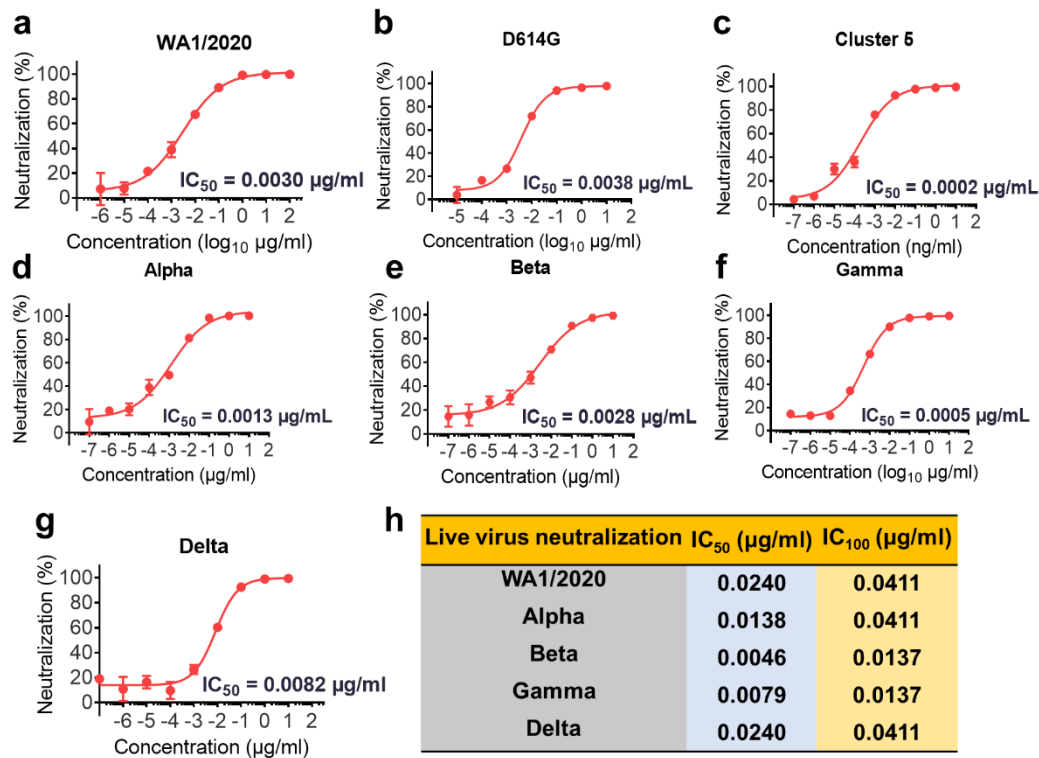
Fig. 4 Extensive neutralization of 2G1 against SARS-CoV-2 variants. a-g, Neutralization of 2G1 to diverse SARS-CoV-2 pseudoviruses. Pseudoviruses with active titer higher than 1×10^7 TU/mL were employed in this study. Concentration-dependent neutralization of 2G1 was quantified by detecting the fluorescence from the luciferase reporter. Data in duplicate are displayed as mean ± S.D. **h,** Live virus neutralization by 2G1. 100 TCID50 of SARS-CoV-2 (WA1/2020, Alpha, Beta, gamma and Delta) were incubated with threefold-diluted 2G1 and then added to Vero E6 cells. After a 3-day incubation, cytopathic effect (CPE) was assessed by counting the plaque formation.

765
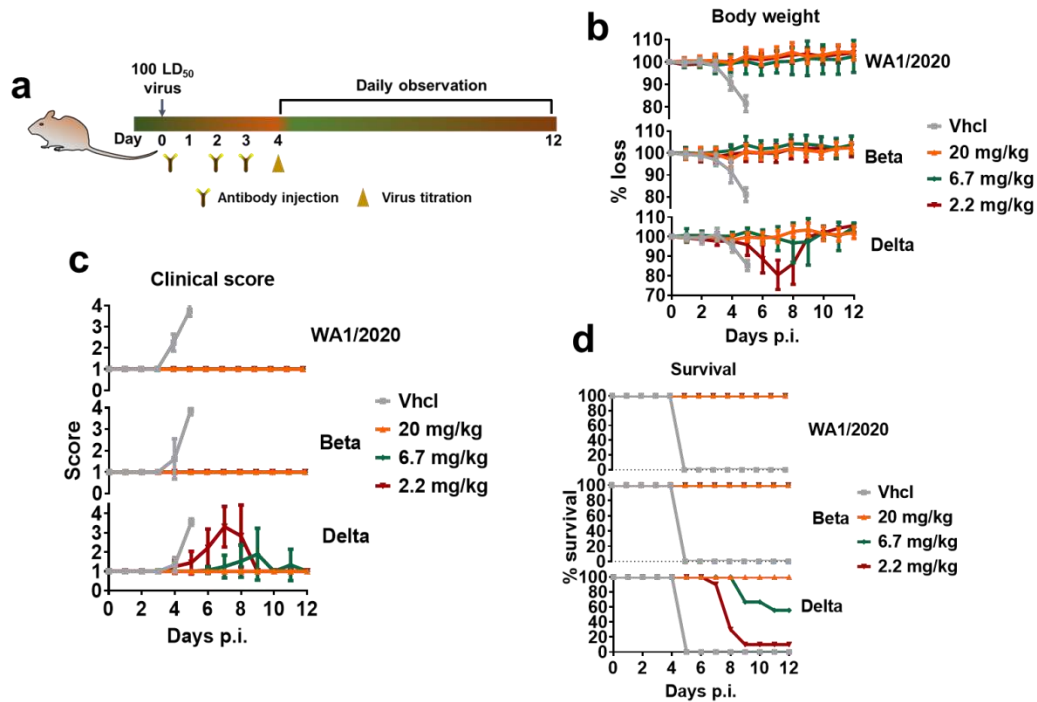
Fig. 5 Therapeutic efficacy of 2G1 against SARS-CoV-2 variants in transgenic mice.
a, High permissive AC70 human ACE2 transgenic mice were challenged with 100 LD_{50} of
SARS-CoV-2 WA1/2020, Beta- or Delta- variants, followed by 20, 6.7, or 2.2 mg/kg of 2G1
treatment (n = 14). A 12-day clinical observation was implemented. **b,** Body weight change
of mice. **c,** Clinical illness of mice was assessed based on a standardized 1 to 4 grading
system that describes the clinical wellbeing of mice. **d,** Mortality of mice. Data are shown
as mean ± S.D. Vhcl, vehicle control; p.i., post infection.
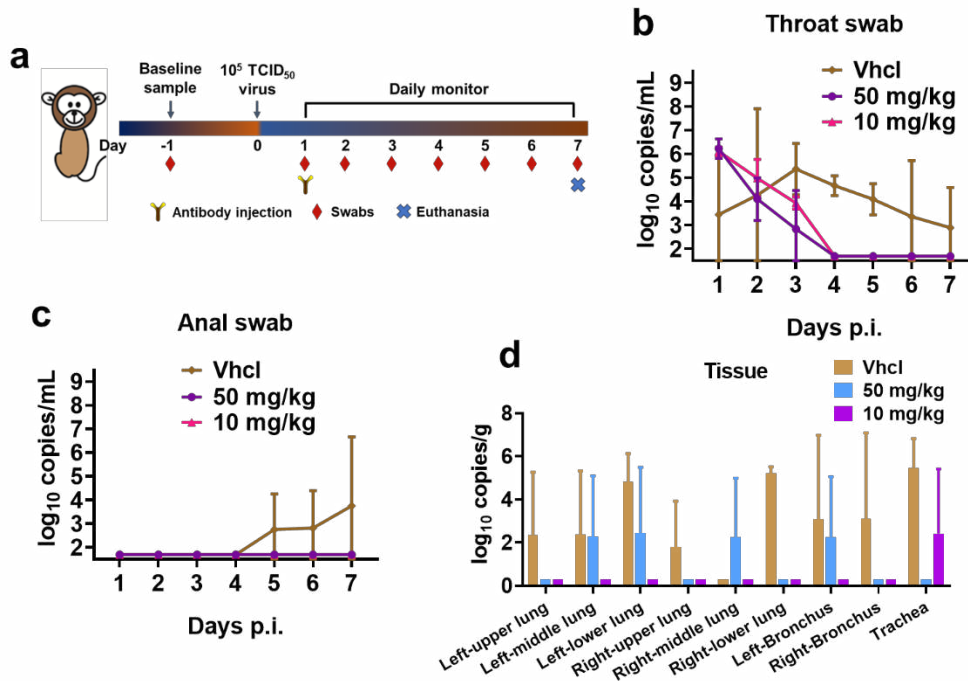
Fig. 6 Therapeutic efficacy of 2G1 against SARS-CoV-2 variants in rhesus macaques. **a,** One male and one female rhesus macaques in each group were endotracheally challenged with 1×10^5 TCID50 of SARS-CoV-2. 2G1 at 10 mg/kg or 50 mg/kg, or equal amount of PBS were intravenously given at 1 dpi. Throat and anal swabs were sampled daily until 7 dpi. **b,** Viral load in throat swab. **c,** Viral load in anal swab. **d,** Viral load in lungs, tracheas, and bronchi. Data with duplications are shown as mean ± S.D. p.i., post infection.
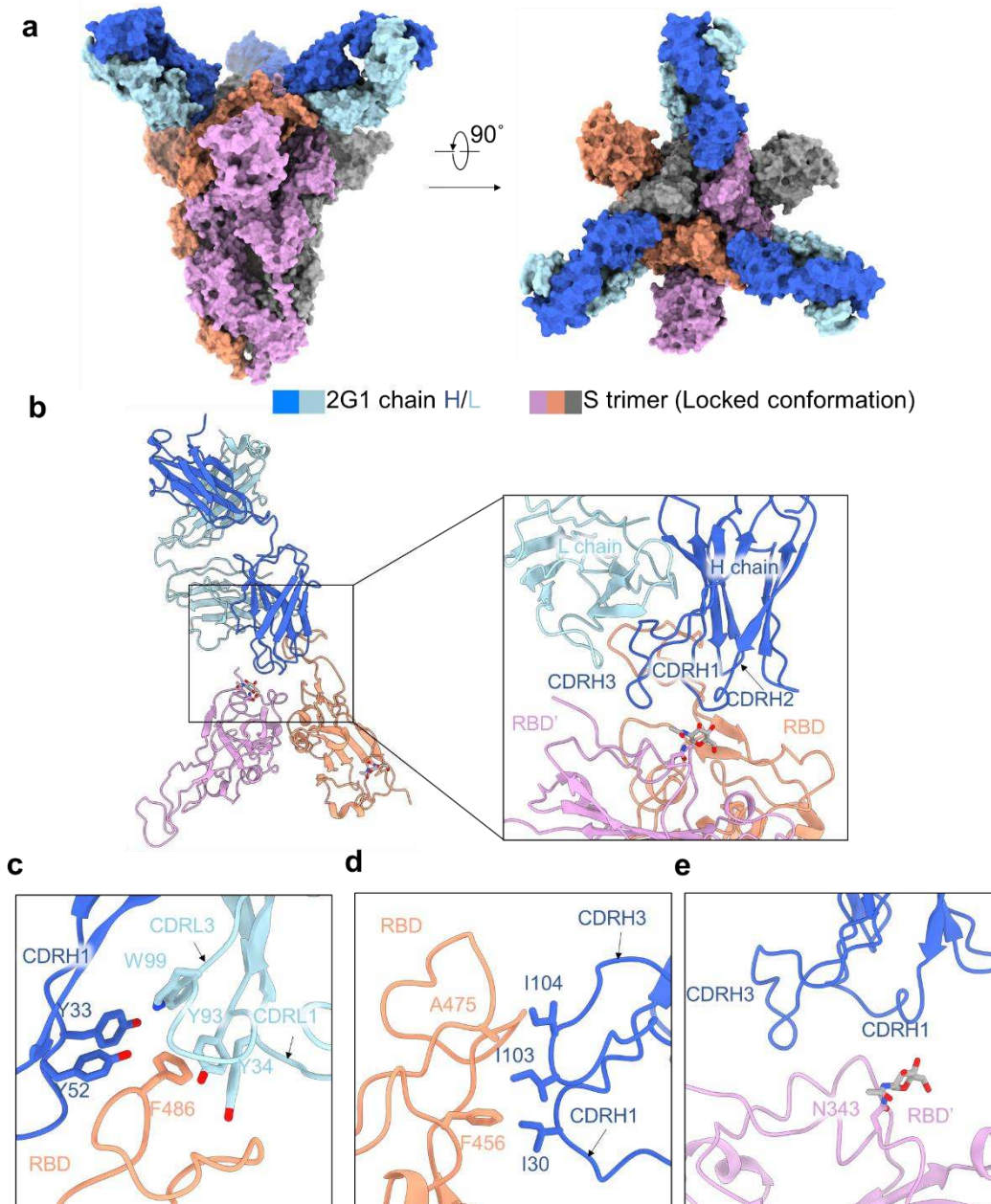
Fig. 7 Cryo-EM structure of 2G1 and the complex with WA1/2020 S protein. a, The domain-colored cryo-EM map of SARS-CoV-2 S ectodomain trimer and 2G1 Fab fragments complex is shown, viewed along two perpendicular orientations. The heavy and light chains of 2G1 are colored blue and cyan, respectively. **b,** The three protomer of trimeric S protein are colored grey, orange and pink. **c-e,** The binding interface between 2G1 and RBD and adjacent RBD'. RBD and 2G1 interact each other mainly through hydrophobic interactions (**c** and **d**). 2G1 heavy chain (CDRH3 and CDRH1) lie above the adjacent RBD' (**e**).
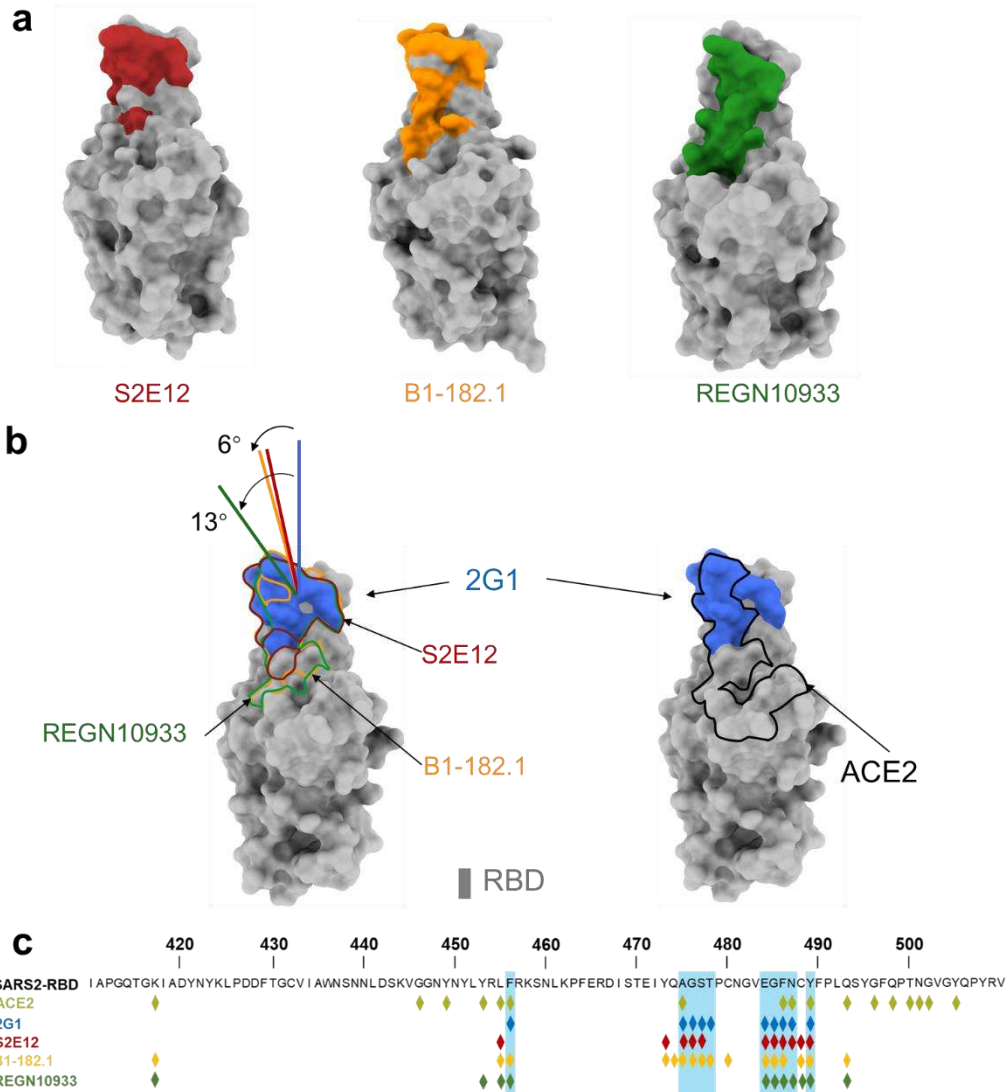
Fig. 8 Analysis of different binding modes of 2G1, S2E12, B1-182.1 and REGN10933. a, The epitope surfaces of S2E12, B1-182.1 and REGN10933 on S protein are in red, orange and green, respectively. **b,** Comparison of binding modes of 2G1, S2E12, B1-182.1 and REGN10933. The epitope surface of 2G1 is in blue. The borderlines of ACE2-binding site, S2E12, B1-182.1 and REGN10933 are shown in black, red, orange and green respectively. The connecting lines between the center of 2G1 Fab and RBD is taken as the principal axis, and axis of Fab S2E12, B1-182.1 are rotated 6° and REGN10933 is rotated 13° approximately. **c,** Mapping of S2E12, B1-182.1 and REGN10933 epitopes on RBD.
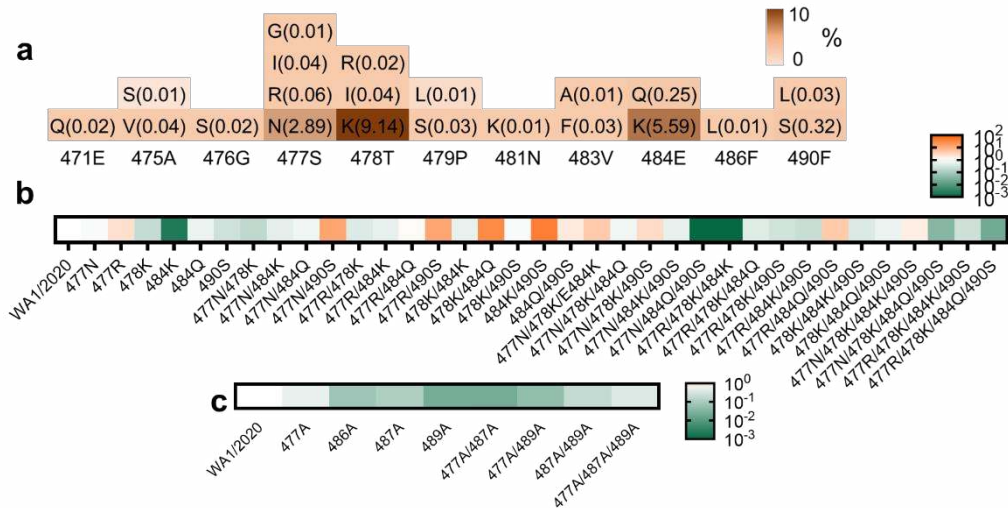
Fig. 9 Identification of critical binding residues for 2G1. a, Statistics of mutation proportion in RBD residue 471Glu - 490Phe where key for 2G1 epitope from GISAID database as of August 2021. **b,** Identification of critical binding residues for 2G1. Spike genes with high frequency mutation sites between 471Glu and 490Phe (>0.05%) were cloned and transiently expressed on the surface of 293T cells. The binding ability of 2G1 to these mutant S proteins was measured by flow cytometry. The fold change of binding ability was normalized by comparing to WA1/2020 S protein. **c,** Mutations in the key interaction sites of 2G1 that affects the binding ability of 2G1 to varying degrees.
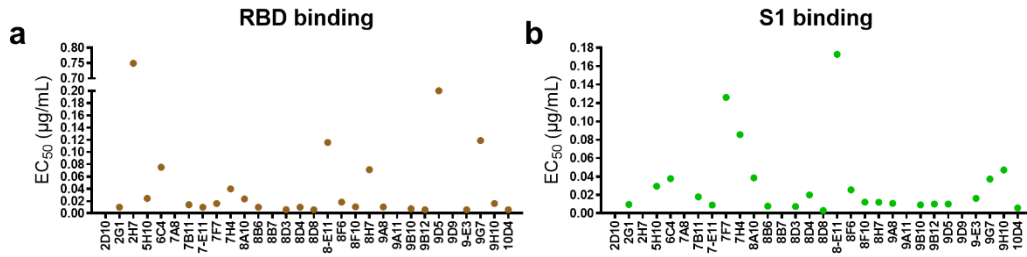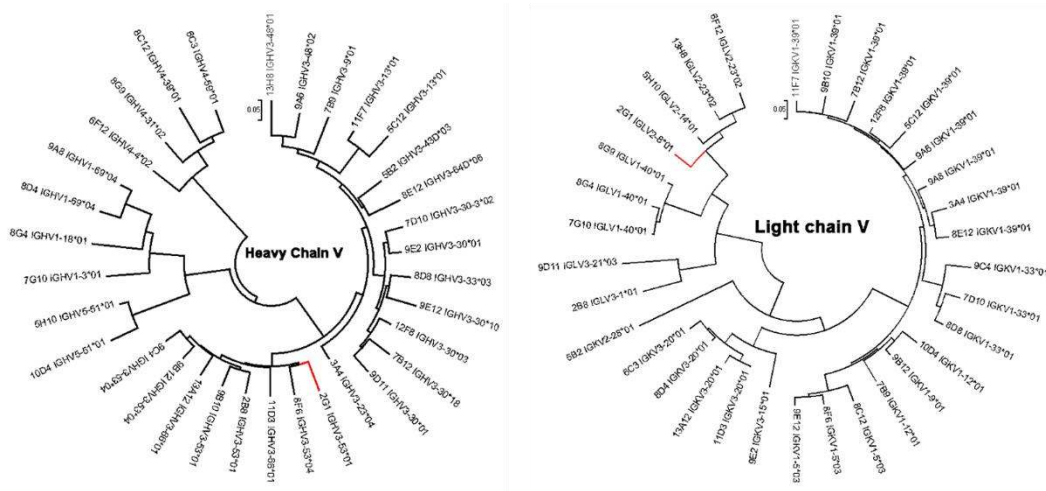
Fig. S1 Evaluation of binding and neutralization of selected antibody candidates. a-b, Candidates' EC_{50} in the concentration-dependent RBD (**a**) and S1 (**b**) binding test using ELISA. Antigens were 3-fold serially diluted from 0.300 μg/mL to 0.0012 μg/mL.
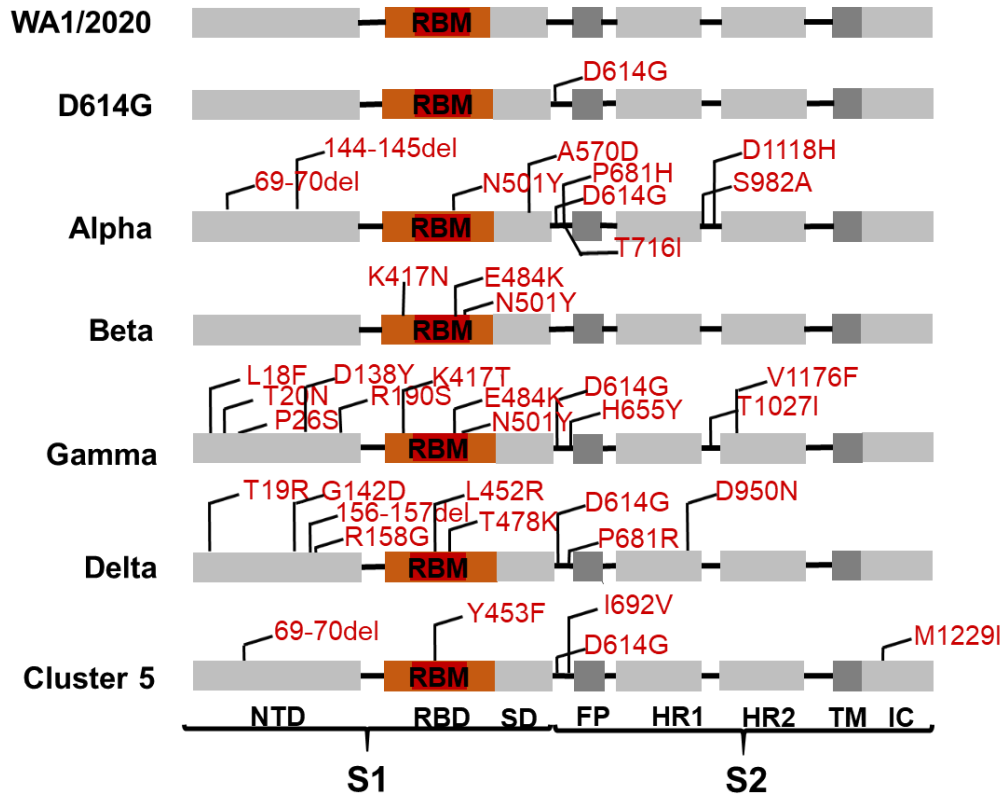

Fig. S2 Germline identification of VH and VL. Germline gene distribution of the heavy chain and light chain of 33 candidates and their clustering analysis.

26

Fig. S3 Mutational sites of pseudoviruses used in this report. The spike region of SARS-CoV-2 is displayed in different modules. The mutation sites are annotated in corresponding positions in detail. RBD is highlighted in saffron yellow and RBM is highlighted in red. NTD, N-terminal domain; RBD, receptor binding domain; RBM, receptor binding motif; SD, subdomain; FP, fusion peptide; HR1, heptad repeats 1; HR2, heptad repeats 2; TM, transmembrane region; IC, intracellular region.
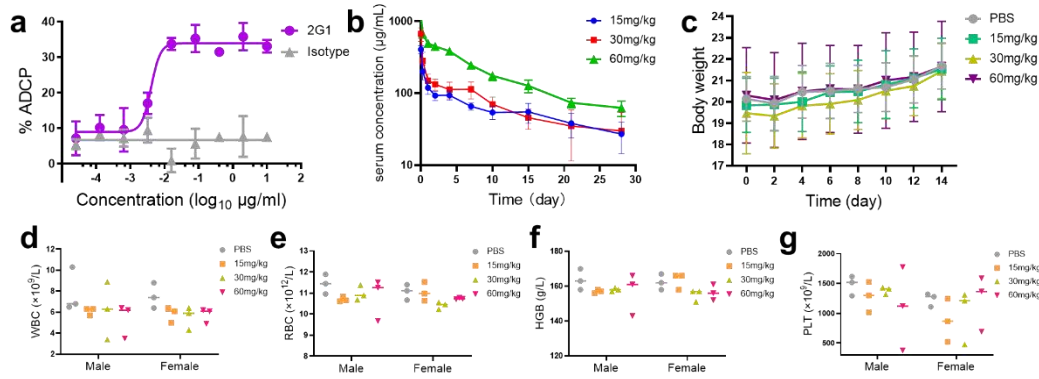
Fig. S4 2G1 induces cellular phagocytosis but no evident adverse effects. a, Antibody-dependent cellular phagocytosis (ADCP) induced by 2G1. Jurkat cells with stable S expression were incubated with macrophages in the presence of different concentrations of 2G1. After incubating at 37℃ for 30 mins, the proportion of Jurkat cells phagocytosed by macrophages was detected by flow cytometry. **b,** Pharmacokinetic study of 2G1. BALB/c mice were treated with different doses of 2G1, and blood samples were collected at different time points. The serum concentration of 2G1 was measured by ELISA. **c-g,** Adverse effect study of 2G1. Crlj:CD1(ICR) mice were treated with different doses of 2G1. Body weight of mice was tracked (**c**). The blood routine indexes including WBC (**d**), RBC (**e**), HGB (**f**), and PLT (**g**) were measured 14 days later. WBC, white blood cell count; RBC, red blood cell count; HGB, hemoglobin; PLT, platelets. Data are presented as mean ± S.D.
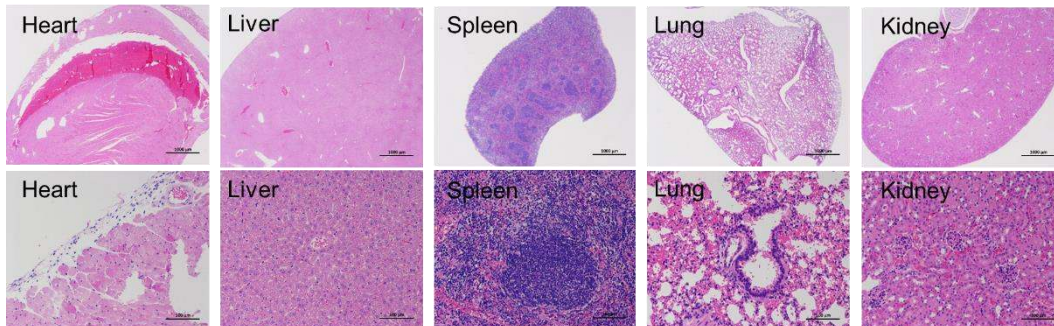
Fig. S5 Organ toxicity study. Crlj:CD1(ICR) mice were treated with 15, 30, or 60 mg/kg of 2G1. Inflammatory damage of hearts, livers, spleens, lungs and kidneys were checked by hematoxylin-eosin (HE) staining. No apparent pathological changes were observed. Representative sections from 60 mg/kg group are displayed.

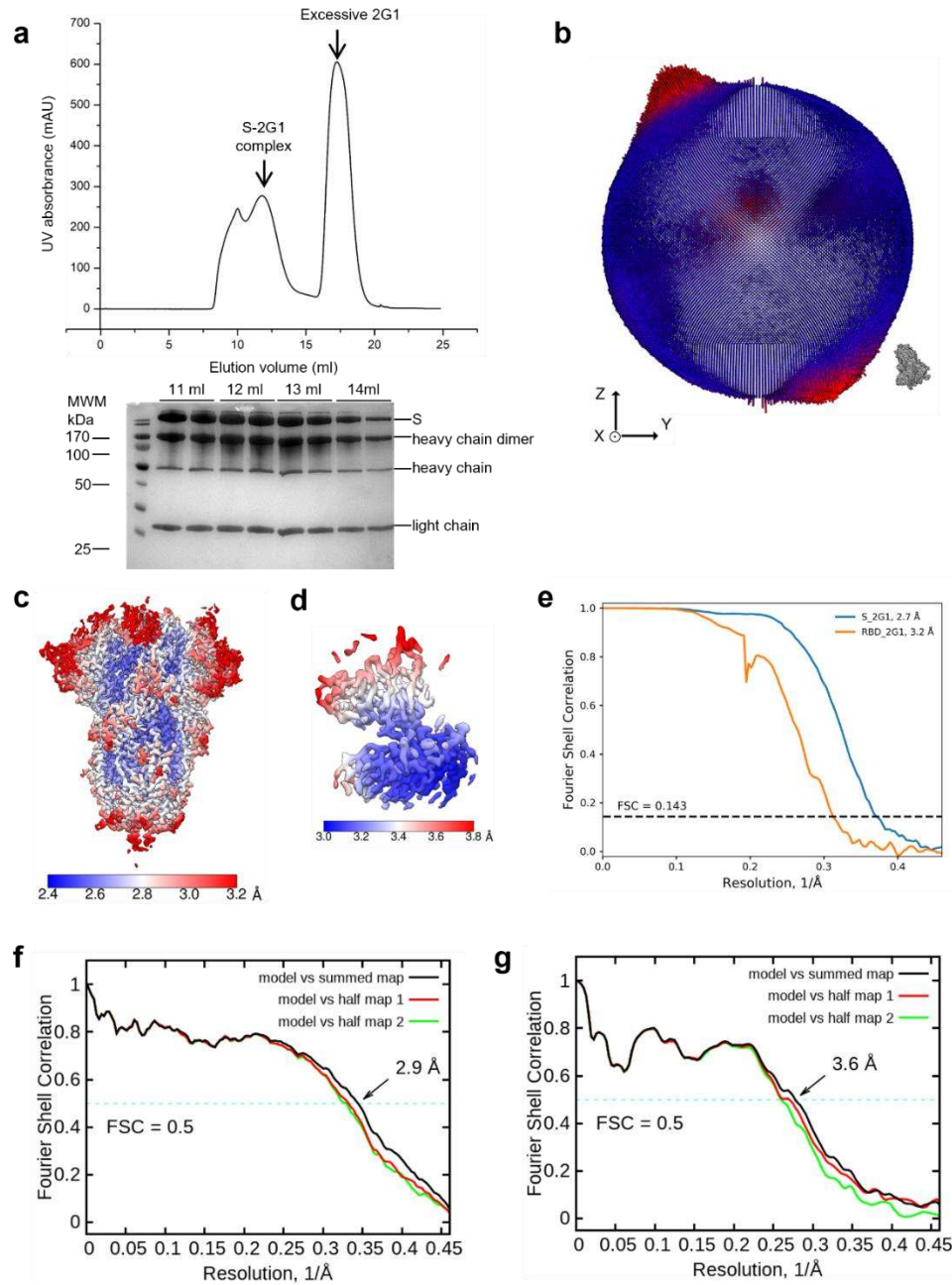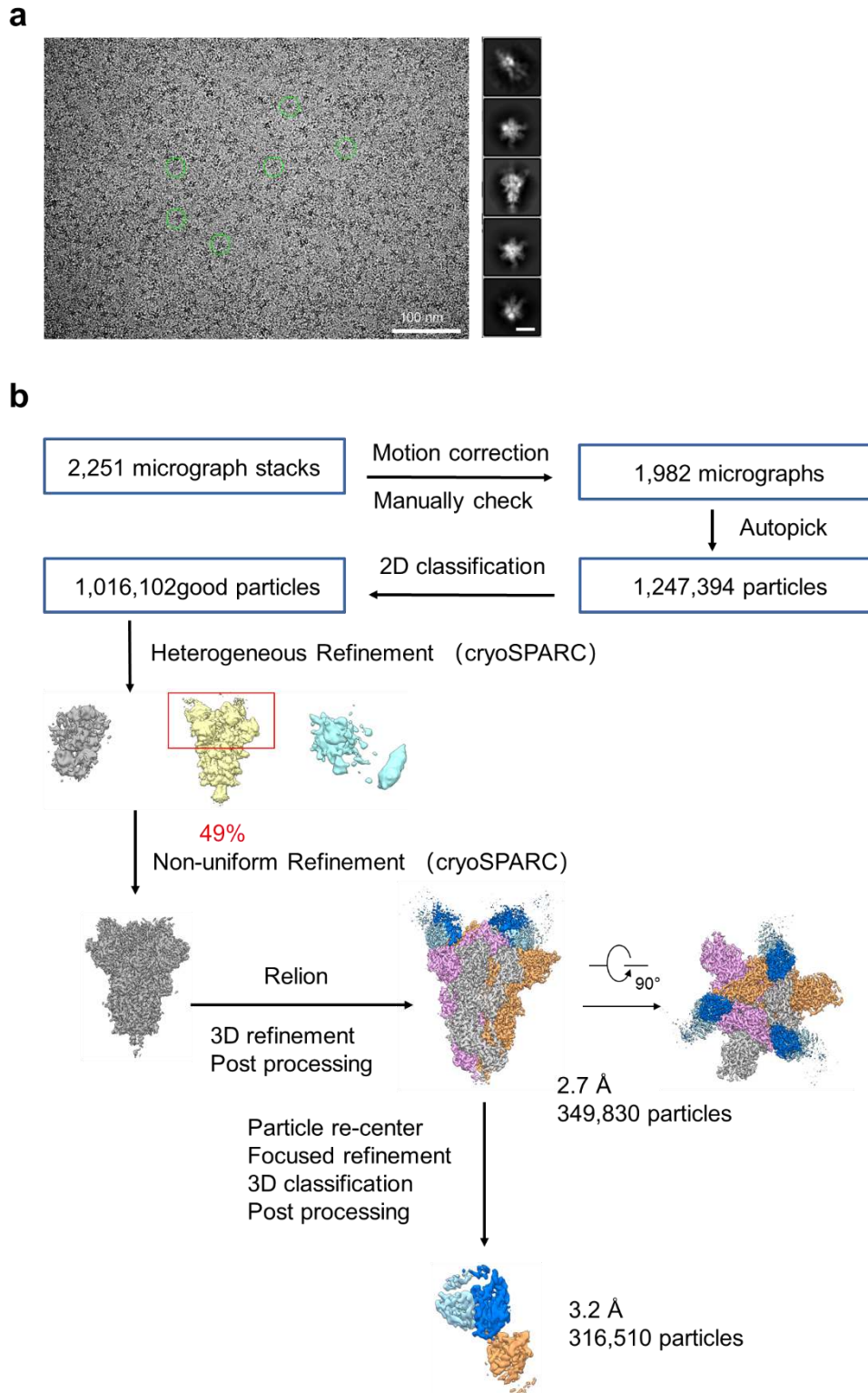**Fig. S6 Cryo-EM analysis of SARS-CoV-2 S trimer in complex with 2G1. a,** Representative gel filtration chromatography purification profile of the SARS-CoV-2 S extracellular domain in complex with 2G1. **b**, Euler angle distribution in the final 3D reconstruction of S bound with 2G1. **c-d,** Local resolution map for the 3D reconstruction of overall structure and RBD-2G1 sub-complex, respectively. **e,** FSC curve of the overall structure (blue) and RBD-2G1 sub-complex (orange). **f,** FSC curve of the refined model of S bound with 2G1 versus the overall structure that it is refined against (black); of the model refined against the first half map versus the same map (red); and of the model refined against the first half map versus the second half map (green). The small difference between the red and green curves indicates that the refinement of the atomic coordinates did not suffer from overfitting. **g,** FSC curve of the refined model of RBD-2G1 sub-complex, which is same to the **f**.

29

912

Fig. S7 Flowchart for cryo-EM data processing of SARS-CoV-2 S trimer in complex with 2G1. a, Representative cryo-EM micrograph and 2D class averages of cryo-EM particle images of **SARS-CoV-2 S trimer** bound with 2G1. The scale bar in 2D class averages is 10 nm. **b,** Please refer to the 'Data Processing' in Methods section for details.

919 **Table S1 Data collection, 3D reconstruction and model statistic.**

Data collection		
EM equipment	Titan Krios (Thermo Fisher Scientific)	
Voltage (kV)	300	
Detector	Gatan K3 Summit	
Energy filter	Gatan GIF Quantum, 20 eV slit	
Pixel size (Å)	1.087	
Electron dose (e-/Å2)	50	
Defocus range (μm)	-1.2 ~ -2.2	
Number of collected micrographs	2,251	
Number of selected micrographs	1,982	
Sample	S protein in complex with 2G1	
3D Reconstruction		
	Whole model	Interface between RBD and 2G1
Software	cryoSPARC/ Relion	Relion
Number of used particles	349,830	316,510
Resolution (Å)	2.7	3.2
Symmetry	C1	
Map sharpening B factor (Å^2)	-90	
Refinement		
Software	Phenix	
Cell dimensions (Å)	313.056	
Model composition		
Protein residues	4,572	
Side chains assigned	4,572	
Sugar	78	
Linoleic acid	3	
R.m.s deviations		
Bonds length (Å)	0.007	
Bonds Angle (°)	0.936	
Ramachandran plot statistics (%)		
Preferred	93.61	
Allowed	6.16	
Outlier	0.23	

920
921
922
923
924
925
926
927
928
929
930
931

References

1   Volz, E. *et al.* Assessing transmissibility of SARS-CoV-2 lineage B.1.1.7 in England. *Nature* **593**, 266-269 (2021).

2   Alpert, T. *et al.* Early introductions and transmission of SARS-CoV-2 variant B.1.1.7 in the United States. *Cell* **184**, 2595-2604 (2021).

3   Liu, J. *et al.* BNT162b2-elicited neutralization of B.1.617 and other SARS-CoV-2 variants. *Nature* **596**, 273-275 (2021).

4   Dejnirattisai, W. *et al.* Antibody evasion by the P.1 strain of SARS-CoV-2. *Cell* **184**, 2939-2954.e2939 (2021).

5   Chen, R. E. *et al.* In vivo monoclonal antibody efficacy against SARS-CoV-2 variant strains. *Nature* **596**, 103-108 (2021).

6   Li, B. *et al.* Viral infection and transmission in a large, well-traced outbreak caused by the SARS-CoV-2 Delta variant. *medRxiv*, doi:10.1101/2021.07.07.21260122 (2021).

7   Andreano, E. & Rappuoli, R. SARS-CoV-2 escaped natural immunity, raising questions about vaccines and therapies. *Nat Med* **27**, 759-761 (2021).

8   Cohen, A. A. *et al.* Mosaic nanoparticles elicit cross-reactive immune responses to zoonotic coronaviruses in mice. *Science* **371**, 735-741 (2021).

9   Ju, B. *et al.* Human neutralizing antibodies elicited by SARS-CoV-2 infection. *Nature* **584**, 115-119 (2020).

10   Lv, Z. *et al.* Structural basis for neutralization of SARS-CoV-2 and SARS-CoV by a potent therapeutic antibody. *Science* **369**, 1505-1509 (2020).

11   Chi, X. *et al.* A neutralizing human antibody binds to the N-terminal domain of the Spike protein of SARS-CoV-2. *Science* **369**, 650-655 (2020).

12   Liu, Z. M. *et al.* Identification of SARS-CoV-2 spike mutations that attenuate monoclonal and serum antibody neutralization. *Cell Host Microbe* **29**, 477-488 (2021).

13   Chen, R. E. *et al.* Resistance of SARS-CoV-2 variants to neutralization by monoclonal and serum-derived polyclonal antibodies. *Nat Med* **27**, 717-726 (2021).

14   Garcia-Beltran, W. F. *et al.* Multiple SARS-CoV-2 variants escape neutralization by vaccine-induced humoral immunity. *Cell* **184**, 2372-2383 (2021).

15   Gupta, R. K. Will SARS-CoV-2 variants of concern affect the promise of vaccines? *Nat Rev Immunol* **21**, 340-341 (2021).

16   Kannan, S., Shaik Syed Ali, P. & Sheeza, A. Evolving biothreat of variant SARS-CoV-2 - molecular properties, virulence and epidemiology. *Eur Rev Med Pharmacol Sci* **25**, 4405-4412 (2021).

17   Bal, A. *et al.* Two-step strategy for the identification of SARS-CoV-2 variant of concern 202012/01 and other variants with spike deletion H69-V70, France, August to December 2020. *Euro Surveill* **26**, 2100008 (2021).

18   Wang, P. F. *et al.* Antibody resistance of SARS-CoV-2 variants B.1.351 and B.1.1.7. *Nature* **593**, 130-135 (2021).

19   Collier, D. A. *et al.* Sensitivity of SARS-CoV-2 B.1.1.7 to mRNA vaccine-elicited antibodies. *Nature* **593**, 136-141 (2021).

20   Andreano, E. *et al.* SARS-CoV-2 escape in vitro from a highly neutralizing COVID-19 convalescent plasma. *bioRxiv*, doi:10.1101/2020.12.28.424451 (2020).

21   Madhi, S. A. *et al.* Efficacy of the ChAdOx1 nCoV-19 Covid-19 Vaccine against the B.1.351 Variant. *N Engl J Med* **384**, 1885-1898 (2021).

976   22   Zhou, D. *et al.* Evidence of escape of SARS-CoV-2 variant B.1.351 from natural and vaccine-
977   induced sera. *Cell* **184**, 2348-2361 (2021).
978   23   Alter, G. *et al.* Immunogenicity of Ad26.COV2.S vaccine against SARS-CoV-2 variants in humans.
979   *Nature* **596**, 268-272 (2021).
980   24   Hoffmann, M. *et al.* SARS-CoV-2 variants B.1.351 and P.1 escape from neutralizing antibodies.
981   *Cell* **184**, 2384-2393 (2021).
982   25   Planas, D. *et al.* Reduced sensitivity of SARS-CoV-2 variant Delta to antibody neutralization.
983   *Nature* **596**, 276-280 (2021).
984   26   Augusto, G. *et al.* In vitro data suggest that Indian variant B.1.617 of SARS-CoV-2 escapes
985   neutralization by both receptor affinity and immune evasion. *Allergy*, doi:10.1111/all.15065
986   (2021).
987   27   Liu, C. *et al.* Reduced neutralization of SARS-CoV-2 B.1.617 by vaccine and convalescent serum.
988   *Cell* **184**, 4220-4236 (2021).
989   28   Padilla-Rojas, C. *et al.* Genomic analysis reveals a rapid spread and predominance of lambda
990   (C.37) SARS-COV-2 lineage in Peru despite circulation of variants of concern. *J Med Virol*,
991   doi:10.1002/jmv.27261 (2021).
992   29   Laiton-Donato, K. *et al.* Characterization of the emerging B.1.621 variant of interest of SARS-
993   CoV-2. *Infect Genet Evol* **95**, 105038 (2021).
994   30   Gomez, C. E., Perdiguero, B. & Esteban, M. Emerging SARS-CoV-2 Variants and Impact in Global
995   Vaccination Programs against SARS-CoV-2/COVID-19. *Vaccines-Basel* **9**, doi:ARTN 243
996   10.3390/vaccines9030243 (2021).
997   31   Harvey, W. T. *et al.* SARS-CoV-2 variants, spike mutations and immune escape. *Nat Rev*
998   *Microbiol* **19**, 409-424, doi:10.1038/s41579-021-00573-0 (2021).
999   32   Yuan, M. *et al.* Structural basis of a shared antibody response to SARS-CoV-2. *Science* **369**, 1119-
1000   1123 (2020).
1001 33   Toelzer, C. *et al.* Free fatty acid binding pocket in the locked structure of SARS-CoV-2 spike
1002   protein. *Science* **370**, 725-730, doi:10.1126/science.abd3255 (2020).
1003 34   Walls, A. C. *et al.* Structure, Function, and Antigenicity of the SARS-CoV-2 Spike Glycoprotein.
1004   *Cell* **181**, 281-292 (2020).
1005 35   Cai, Y. F. *et al.* Structural basis for enhanced infectivity and immune evasion of SARS-CoV-2
1006   variants. *Science* **373**, 642-648 (2021).
1007 36   Liu, Y. & Rocklöv, J. The reproductive number of the Delta variant of SARS-CoV-2 is far higher
1008   compared to the ancestral SARS-CoV-2 virus. *J Travel Med*, doi:10.1093/jtm/taab124 (2021).
1009 37   Hoffmann, M. *et al.* SARS-CoV-2 variant B.1.617 is resistant to bamlanivimab and evades
1010   antibodies induced by infection and vaccination. *Cell Rep* **36**, 109415 (2021).
1011 38   Lopez Bernal, J. *et al.* Effectiveness of Covid-19 Vaccines against the B.1.617.2 (Delta) Variant.
1012   *N Engl J Med* **385**, 585-594 (2021).
1013 39   Hsieh, C. L. *et al.* Structure-based design of prefusion-stabilized SARS-CoV-2 spikes. *Science* **369**,
1014   1501-1505 (2020).
1015 40   Lei, J. & Frank, J. Automated acquisition of cryo-electron micrographs for single particle
1016   reconstruction on an FEI Tecnai electron microscope. *J Struct Biol* **150**, 69-80 (2005).
1017 41   Zheng, S. Q. *et al.* MotionCor2: anisotropic correction of beam-induced motion for improved
1018   cryo-electron microscopy. *Nat Methods* **14**, 331-332 (2017).
1019 42   Grant, T. & Grigorieff, N. Measuring the optimal exposure for single particle cryo-EM using a

1020		2.6 angstrom reconstruction of rotavirus VP6. *Elife* **4**, e06980 (2015).
1021	43	Zhang, K. Gctf: Real-time CTF determination and correction. *Journal of Structural Biology* **193**,
1022		1-12 (2016).
1023	44	Zivanov, J. *et al.* New tools for automated high-resolution cryo-EM structure determination in
1024		RELION-3. *Elife* **7**, e42166 (2018).
1025	45	Kimanius, D., Forsberg, B. & Lindahl, E. Accelerated Cryo-EM Structure Determination with
1026		Parallelisation using GPUs in Relion-2. *Elife* **5**, e18722 (2016).
1027	46	Scheres, S. H. W. RELION: Implementation of a Bayesian approach to cryo-EM structure
1028		determination. *Journal of Structural Biology* **180**, 519-530 (2012).
1029	47	Scheres, S. H. W. A Bayesian View on Cryo-EM Structure Determination. *J Mol Biol* **415**, 406-
1030		418 (2012).
1031	48	Punjani, A., Rubinstein, J. L., Fleet, D. J. & Brubaker, M. A. cryoSPARC: algorithms for rapid
1032		unsupervised cryo-EM structure determination. *Nature Methods* **14**, 290-296 (2017).
1033	49	Rosenthal, P. B. & Henderson, R. Optimal determination of particle orientation, absolute hand,
1034		and contrast loss in single-particle electron cryomicroscopy. *J Mol Biol* **333**, 721-745 (2003).
1035	50	Chen, S. X. *et al.* High-resolution noise substitution to measure overfitting and validate
1036		resolution in 3D structure determination by single particle electron cryomicroscopy.
1037		*Ultramicroscopy* **135**, 24-35 (2013).
1038	51	Trabuco, L. G., Villa, E., Mitra, K., Frank, J. & Schulten, K. Flexible fitting of atomic structures
1039		into electron microscopy maps using molecular dynamics. *Structure* **16**, 673-683 (2008).
1040	52	Winn, M. D. *et al.* Overview of the CCP4 suite and current developments. *Acta Crystallogr D* **67**,
1041		235-242 (2011).
1042	53	Emsley, P., Lohkamp, B., Scott, W. G. & Cowtan, K. Features and development of Coot. *Acta
1043		Crystallographica Section D-Biological Crystallography* **66**, 486-501 (2010).
1044	54	Adams, P. D. *et al.* PHENIX: a comprehensive Python-based system for macromolecular
1045		structure solution. *Acta Crystallogr D Biol Crystallogr* **66**, 213-221 (2010).
1046		
1047		
1048		